Model Intercomparison of the Impacts of Varying Cloud Droplet Nucleating Aerosols on the Lifecycle and Microphysics of Isolated Deep Convection

Stephen M. Saleeby[a], Susan C. van den Heever[a], Peter J. Marinescu[a], Mariko Oue[b], Andrew I. Barrett[c], Christian Barthlott[c], Ribu Cherian[d,n], Jiwen Fan[e,p], Ann M. Fridlind[f], Max Heikenfeld[g], Corinna Hoose[c], Toshi Matsui[h,i], Annette K. Miltenberger[j,k], Johannes Quaas[d], Jacob Shpund[e,o], Philip Stier[g], Benoit Vie[l], Bethan A. White[g,m], and Yuwei Zhang[e]

[a] *Department of Atmospheric Science, Colorado State Univ., Fort Collins, CO, USA*

[b] *School of Marine and Atmospheric Sciences, Stony Brook Univ., Stony Brook, NY, USA*

[c] *Institute of Meteorology and Climate Research Troposphere Research (IMKTRO), Karlsruhe Institute of Technology, Karlsruhe, Germany*

[d] *Institute for Meteorology, Leipzig University, Leipzig, Germany*

[e] *Pacific Northwest National Laboratory, Richland, WA, USA*

[f] *NASA Goddard Institute for Space Studies, New York, NY, USA*

[g] *Atmospheric, Oceanic and Planetary Physics, Dept. of Physics, University of Oxford, Oxford, UK*

[h] *NASA Goddard Space Flight Center, Greenbelt, MD, USA*

[i] *Earth System Science Interdisciplinary Center, University of Maryland, College Park, MD*

[j] *School of Earth and Environment, University of Leeds, Leeds, UK*

[k] *Institute for Atmospheric Physics, Johannes Gutenberg University, Mainz, Germany*

[l] *CNRM, Université de Toulouse, Météo-France, CNRS, Toulouse, France*

[m] *Bureau of Meteorology, Melbourne, Victoria, Australia*

[n] *Centre for Earth & Atmospheric Sciences, Sathyabama Institute of Science and Technology, Chennai, India*

[o] *Institute of Earth sciences, Dept of Atmospheric sciences, Hebrew University of Jerusalem, Israel*

[p] *Argonne National Laboratory, Lemont, IL, USA*

Corresponding author: Stephen M. Saleeby, Stephen.Saleeby@colostate.edu

ABSTRACT

The microphysical impacts of aerosol particles on scattered isolated deep convective cells near Houston, Texas on 19 June 2013, are examined using multiple cloud-system resolving model (CRM) simulations initialized with vertical profiles of low and high concentrations of cloud droplet nucleating aerosols. These simulations formed part of the Model Intercomparison Project (MIP) conducted by the Deep Convective Working Group of the Aerosol, Cloud, Precipitation and Climate (ACPC) initiative. Each CRM generated a field of convective cells representing those observed during the case study with varying degrees of accuracy. The Tracking and Object-Based Analysis of Clouds (*tobac*) cell tracking algorithm was applied to each MIP CRM simulation to track relatively long-lived convective cells (20-60 minutes). Most of the CRMs produced similar aerosol loading impacts on the warm-phase of tracked cell properties with reduced autoconversion and accretion growth of rain, increased cloud water, reduced rainfall, and reduced near-surface evaporation of rain. The sign of aerosol impacts on the warm-phase properties of the convective cells was also quite consistent over cell lifetimes with the greatest magnitude of influence in the first half of the lifecycle in most CRMs. In contrast, the ice-phase response to aerosol loading was highly variable amongst CRMs and included increases or decreases in ice amounts at inconsistent stages of cell lifecycle and mid-level vs upper-level changes in ice. This inter-model variability in ice is indicative both of the complex indirect interactions between aerosols and ice-phase processes in deep convection and their associated parameterizations.

1. Introduction

Cloud droplet nucleating aerosols are an essential component to cloud formation via their role as cloud condensation nuclei. Increases in the aerosol number concentration have been shown to increase cloud albedo (Twomey, 1977), reduce cloud precipitation efficiency, and increase cloud lifetime (Albrecht, 1989) through the generation of more numerous but smaller cloud droplets in shallow clouds (e.g., Twomey and Squires, 1959; Kaufman and Nakajima, 1993). A population of more numerous, smaller cloud droplets leads to delayed autoconversion and accretion growth of precipitating sized raindrops due to the reduced collision-coalescence efficiency of smaller droplets and narrowing of the droplet spectrum (e.g., Squires 1958; Rosenfeld, 1999; Pinsky et al., 2008; Tao et al., 2012). Such clouds may persist for longer periods of time, continue to grow by vapor condensation, and permit lofting of cloud droplets to higher altitudes since they are less efficiently scavenged (e.g., Rosenfeld and Woodley, 2000; Khain et al., 2004; van den Heever et al., 2006; Altaratz et al., 2014; Koren et al., 2014; Saleeby et al., 2015). In some cases, extremely high concentrations of aerosols can effectively shut down precipitation formation if the droplet sizes are sufficiently small (Rosenfeld, 1999).

In deep convective clouds, where a variety of hydrometeor growth processes and phases occurs during their lifecycle, aerosols may impact the processes in complex and non-linear ways. In addition to warm-phase impacts of aerosols on cloud microphysics, the mixed-phase riming growth of ice hydrometeors in deep convection is also impacted by aerosol-induced changes to the cloud droplet size distribution. As droplet sizes are reduced, the efficiency with which they contribute to riming growth of ice hydrometeors can be substantially reduced, thus inhibiting ice growth (Lowenthal et al., 2011). Whether riming is enhanced or inhibited by a greater population of smaller cloud droplets is determined by both the size of the droplets and their number concentration. In a high aerosol scenario, if the droplet sizes are not reduced substantially enough to offset the greater number of droplets contributing positively to the collection efficiency between ice hydrometeors and cloud droplets, then greater riming and ice production can result (Khain et al., 2011; Ilotoviz et al., 2016; Saleeby et al., 2016). However, a tipping point towards reduced riming may be reached at very high aerosol concentration (Khain et al., 2011; Ilotoviz et al., 2016; Barrett and Hoose, 2023). Cheng et al. (2010) also showed that riming rates either decrease or increase depending on the compensating impacts of higher droplet number versus smaller droplet size which impacts ice distributions and precipitation in non-linear ways. As

such, we may expect mixed-phase cloud regions to be sensitive to changes in aerosols through the modification of the cloud droplet size distribution and its impact on riming growth of ice.

Previous studies have also shown that an increase in aerosol concentration with corresponding change in the cloud droplet size distributions and enhanced droplet surface areas can lead to changes in the profiles of latent heating in convective clouds (e.g., Khain et al., 2005; Tao et al., 2007; Storer and van den Heever, 2013; Marinescu et al., 2016). Increases in latent heating, and thus buoyancy, have the potential to invigorate and deepen the storms through increases in updraft strength (e.g., Andreae et al., 2044; Koren et al., 2005; Khain et al., 2004, 2005; Tao et al., 2007; Storer and van den Heever, 2013; Koren et al., 2014; Fan et al., 2018).

Aerosol-induced invigoration via changes in latent heating has been hypothesized to occur through several key pathways: *cold phase invigoration* (e.g., Khain et al., 2005; van den Heever et al., 2006; Tao et al., 2007; Rosenfeld et al., 2008; Fan et al., 2012), *condensational invigoration* (e.g., Fan et al., 2007; Saleeby et al., 2015; Sheffield et al., 2015; Grabowski and Morrison, 2016; Igel and van den Heever, 2021), and *humidity-entrainment invigoration* (Abbott and Cronin, 2021). Other studies have indicated mixed or inconsistent results related to aerosol invigoration due to competing processes in deep convection (Morrison and Grabowski, 2011; Fan et al., 2013; Grabowski and Morrison, 2016; Igel and van den Heever, 2021). Further, several recent observational studies (Varble 2018; Veals et al. 2022; Oktem et al., 2023) have been unable to find evidence of convective invigoration in the associated field study locations, though they note the difficulty in isolating aerosol impacts in such complicated environments and the need for focused additional studies. Complex non-linear interactions among aerosols, cloud and ice hydrometeors, latent heating, cold pool forcing and the environmental conditions may all contribute to the ultimate impacts of aerosols on deep convective updrafts and precipitation (e.g., Khain and Pokrovsky, 2004; Khain et al., 2004, 2005; Wang et al., 2005; Teller and Levin, 2006; van den Heever et al., 2006; Cheng et al., 2007; Fan et al., 2007; Storer and van den Heever, 2013; Saleeby et al., 2016; Marinescu et al., 2017; Grabowski and Morrison, 2016; Abbott and Cronin, 2021; Sokolowsky et al., 2022). These complex interactions make it challenging to draw blanket conclusions regarding aerosol impacts on convective updrafts, microphysics, and precipitation.

To more rigorously assess the impacts of aerosols on deep convection from a numerical modeling perspective, Marinescu et al. (2021), hereafter M21, examined the impacts using

simulations from a Model Intercomparison Project (MIP) conducted by the Deep Convective Working Group (van den Heever et al., 2017), hereafter V17, of the Aerosol, Cloud, Precipitation and Climate (ACPC) initiative (Rosenfeld et al., 2014; www.acpcinitiative.org). The ACPC-MIP conducted cloud resolving model simulations focused on the Houston, TX area of the United States for a case of ordinary deep convection simulated from 1200 UTC 19 June to 1500 UTC 20 June 2013 (V17). Simulations with low and high concentrations of cloud droplet nucleating aerosols (hereafter "Low-Aero" and "High-Aero") were run in a nested grid configuration down to 500 m horizontal grid spacing for seven numerical models (presented in Section 2a). The use of an array of different CRMs provides a broad range of simulated responses to aerosol loading that result from differences in parameterizations related to dynamics, microphysics, and subsequent feedbacks and interactions. This analysis of aerosol sensitivity within multiple CRMs will help address the ACPC-MIP goal of determining the range in convective responses to aerosol loading across state-of-the-art modeling frameworks. As such, the results encompass an ensemble of potential convective responses to aerosol loading that may be expected among the atmospheric numerical modeling community. M21 specifically examined the impacts of aerosol concentration on the convective updraft dynamics simulated by these

Model	ICON
Model Version	v2.5.0; Zängl et al., 2015
Grid	Arakawa-C
Vertical Coordinate	SLEVE coordinate implementation (Leuenbergeret al.,2010)
Land Surface	TERRA: Heise et al. (2006)
Boundary Layer / Turbulence	3D turbulence scheme using prognostic TKE (Dipankar et al., 2015)
Radiation	RRTM radiation scheme (Mlawer et al., 1997)
Initial / Boundary Condition Dataset	ECMWF Integrated Forecast System: ECMWF (2016)
Microphysics	2M: Seifert and Beheng (2006a), Seifert et al. (2012)
Hydrometeors	c, r, g, h, s, i; (2M in all hydrometeors)
Hydrometeor Fall Speeds	Number and mass weighted mean fall speeds, varying DSDs and power laws for different hydrometeors
Saturation Adjustment	Yes
Aerosol Activation	Based on Abdul-Razzak & Ghan (2000) scheme
Aerosol Processes	Temporal constant aerosol profile
Heterogeneous Ice Nucleation	Phillips et al. (2008)

Table 1. Details of the varying physical parameterizations in the ICON model. For model hydrometeor classes, c, r, g, h, s, i refer to cloud, rain, graupel, hail, snow and cloud ice.

various CRMs via a detailed analysis of the terms that contribute to the prognostic vertical velocity equation. For an increase in aerosol concentration, they found a consistent increase in vertical velocity within the warm-phase and lower mixed-phase portions of the convective cloud columns, from 4-7 km above ground level (AGL), and highly variable results (increases, decreases, and neutral changes in vertical velocity) in the mid to upper levels of the convection. The increase in vertical velocity (that peaked around the 4.75 km AGL, 0°C level) was largely attributed to enhanced buoyancy (condensational invigoration), though there were likely contributions to condensational heating from environmental feedbacks related to instability.

van den Heever et al. (2025), hereafter V25, provided an overarching view of the aerosol-induced variability in the bulk convective, dynamical and microphysical properties as a function of the CRMs forming part of the MIP. V25 highlights that the model spread in total precipitation tends to be greater than that resulting from aerosol loading within each model, while most models do indicate a reduction in surface precipitation. Further, the sign of cold pool responses to aerosol loading is variable among models, which is likely linked to greater model variability in cold phase microphysics. M21 focused specifically on changes to the convective updrafts due to changes in latent heating associated with microphysical phase changes.

This current companion study examines the same MIP simulations of the convective event as V25 and M21, but it more closely examines the time-varying impact of aerosol loading on the microphysical properties and processes in convective cells and subsequent feedbacks. More specifically, it seeks to identify: (1) similarities and differences in liquid and ice-phase properties and processes (among MIP CRMs and low and high aerosol environments), (2) the corresponding changes to latent heating, (3) the potential feedbacks to the convective updrafts, and (4) the variability of these characteristics over convective cell lifecycles. While M21 provided their updraft analysis of identified convective columns over all domain-space and time of this simulated event, in this study we isolate and track convective cells over time using a cell tracking tool that is discussed in detail below. This method allows us to specifically examine the variations over cell lifetimes of aerosol effects on updrafts and the associated cloud microphysics. This also permits an examination of composites of cell properties, a comparison of cell characteristics (and their variability with aerosol concentration) among the MIP CRMs, and a link between cloud hydrometeors, phase changes, latent heating, and convective updrafts.

2. Models and Methods

a. ACPC MIP Models

The CRMs included in the ACPC-MIP were the: Consortium for Small-scale modeling v5.1 (COSMO; Schättler et al., 2019), Meso-NH Model v5.4.1 (Meso-NH; Lac et al., 2018), Regional Atmospheric Modeling System v6.2.09 (RAMS; Cotton et al. 2003, Saleeby and van den Heever, 2013), Unified Model v10.8 (UM; Walters et al., 2017; Field et al., 2023), NASA Unified Weather Research and Forecasting (WRF) Model v3.9.1 (NU-WRF; Skamarock et al. 2008, Peters-Lidard et al., 2015), WRF v3.7.1 with Morrison microphysics (WRF-Morr; Skamarock et al., 2008), and WRF v4.0.3 with a new version of the Hebrew University Cloud Model bin microphysics (WRF-SBM; Shpund et al., 2019). The details of each of these CRMs, simulation configuration, the physics choices, and the aerosol initial conditions are described in detail in V17 and M21. We briefly note that the maximum aerosol concentrations at the surface were 500 cm^{-3} for "Low-Aero" and 4000 cm^{-3} for "High-Aero" with a log-normal size distribution median diameter of 100 nm and hygroscopicity factor *kappa* of 0.2 (as defined by Petters and Kreidenweis (2007)). The initial vertical profile of aerosol number concentration is given in M21 and is based on both satellite and field program in situ data near Houston for this case on 19 June 2013. The Icosahedral Nonhydrostatic Model (ICON; Zängl et al., 2015) was run after the other MIP CRMs, the results of which are also included here. The ICON model setup, details, physical parameterizations, and associated references are given in Table 1 of this manuscript and can be compared with the rest of those summarized in Table A1 of M21. While the simulation setups between CRMs were kept as similar as possible, the participating CRMs vary in their dynamic cores, vertical coordinates, boundary layer schemes, radiation parameterizations, and microphysics representations. Given the focus of aerosol impacts on convection, it is particularly noteworthy that these CRMs vary in their hydrometeor classes, bulk vs bin microphysics approaches, and explicit activation of aerosols for droplet nucleation versus saturation adjustment approaches.

b. Convective cell identification and filtering

The ACPC MIP simulations' output is available at one-minute output frequency, for the innermost nested domain with 500m horizontal grid spacing, for a 3-hour period (2100 UTC 19 June - 0000 UTC 20 June) of enhanced convective activity (V17). M21 focused on the analysis

of convective columns in a bulk sense following the identification of column updrafts using several dynamic and microphysical criteria. To objectively identify and track distinct convective cells and their associated cloud volumes over their individual lifetimes, we used the Tracking and Object-Based Analysis of Clouds (*tobac*; Heikenfeld et al. 2019a,b) feature identification and tracking algorithm. More specifically, we used *tobac* (v1.2) to identify and track convective cells within the high temporal frequency 1-minute data using similar updraft identification criteria as in Heikenfeld et al. (2019a,b). Convective cells were identified via mid-level (3.5-8.0 km AGL) vertical velocity using multi-threshold criteria with increasing upward velocity of 3, 5, 10 m s^{-1}. More specifically, if an updraft was identified somewhere within a column over the 3.5-8.0 km AGL altitude range and it exceeded the given minimum threshold, then the contiguous group of columns associated with this updraft that meet the threshold is identified as a feature or cell by *tobac*. Cell center locations (grid point location and latitude/longitude locations used for cell tracking) within the defined convective cell updraft regions were determined using centroid measuring techniques. (See Heikenfeld et al. (2019a) for details on the multi-thresholding approach and cell center identification.) A multi-threshold approach permits more specific identification of updraft features under a broader zone of vertical motion while maintaining a minimum distance separation between identified updrafts in order to keep the updraft identification distinct. This approach also permits a separate treatment and analysis of cells of possibly different strengths and microphysical characteristics that may fall under a common updraft region. Cell splits and mergers are not considered in this version of *tobac*, however, given the nature of the convection in this case, splits and mergers are infrequent. Future versions of *tobac* do contain this additional capability (Sokolowsky et al., 2024).

Once cells were identified at each time within the 1-minute output data over the 3-hour simulation period, *tobac* was used to link the identified cells in time to generate cell tracks following the cell center locations. For this study, we filtered the output to retain and analyze only cells which met the following criteria: (1) cells with lifetimes from 20-60 minutes, (2) cells in which an updraft of > 3 m s^{-1} reached higher than 6 km AGL during its lifetime, (3) cells with tracked centers that did not come within 4 km of the lateral boundaries, and (4) cells that completed their lifecycle prior to the final time of 1-min data. These criteria filtered out short-lived, shallow convective cells so that subsequent analyses focus on deep convective cells that

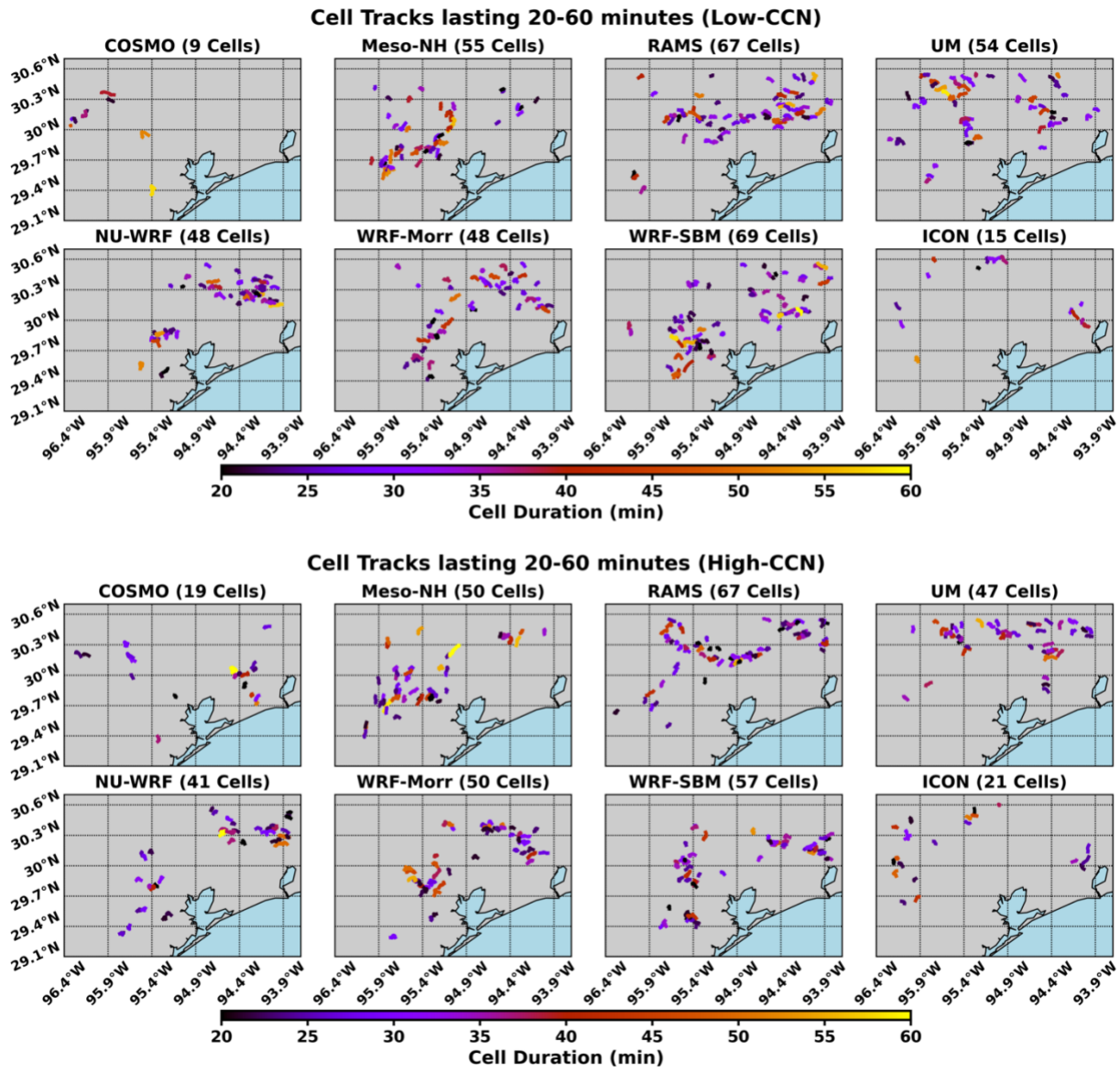

Figure 1. Tracks for cells (from the innermost nested domain) with durations of 20-60 minutes from the Low-Aero simulations (top set of panels) and High-Aero simulations (bottom set of panels). Tracks are denoted by the cell lines while the colors denote the cell lifetimes. The number beside each model's name indicates the number of cells/tracks shown in that panel.

reached well above the 0°C level (~ 4.75 km AGL). Cells lasting less than 20 minutes are unlikely to have time to deepen and generate robust ice microphysics. Only a few cells lasted more than 60 minutes. The cell tracks and lifetimes for the MIP CRMs Low- and High-Aero simulations are shown in Figure 1, while histograms showing the number distribution of cells by lifetime from all simulations are shown in Figure 2. It is apparent that most of the cell lifetimes are on the shorter end of the filtered lifetime range for all CRMs and simulations. Further, there

is greater variability in the number of cells between CRMs than between each CRM's Low- and High-Aero simulations. This variability in numbers of cells and cell lifetimes should be kept in mind when assessing the composite cell analysis that follows.

COSMO has the fewest cells (9) in its Low-Aero run while RAMS (67) and WRF-SBM (69) generate the greatest number of cells in their Low-Aero runs. This is generally in agreement with results from M21, which showed that COSMO tended to produce the least convection (using total precipitation as a metric) among the MIP CRMs, while RAMS and WRF-SBM generated the most (the areal coverage of convection roughly scales with the number of tracked cells). Several of the CRMs produce more (fewer) cells for higher (lower) aerosol concentration, but this trend is not consistent across all CRMs. The number of cells generated is likely tied to many factors including the microphysics, convective initiation, cold pool boundaries, and the complex feedbacks that occur among these factors (e.g., Marinescu et al. 2021).

c. Convective cell analysis criteria

As discussed above, cells have been defined as contiguous updraft regions based on minimum mid-level updraft criteria, and they may vary in size. Shallow warm-phase-only cells have been filtered out given our focus on deep isolated convection. Cell center locations are provided in latitude/longitude coordinates at each time the cell is identified over its lifetime. This cell center information is then used as the anchor location to compute cell characteristics at each

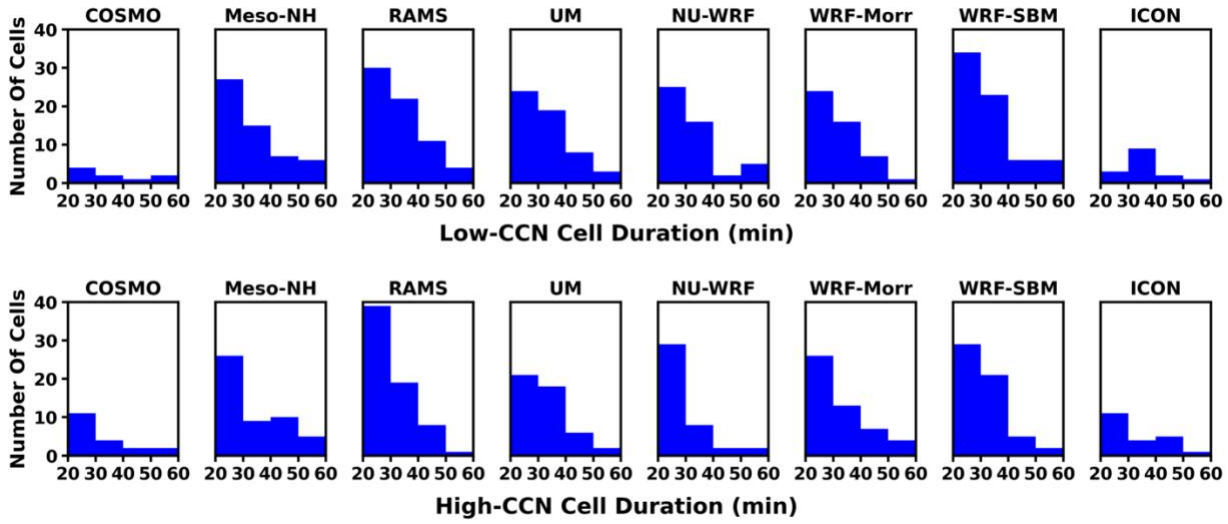

Figure 2. Histograms showing the number of cells in each 10-minute lifetime bin.

time and height over cell lifetimes for all of the MIP simulations. Since cells can span various sizes in space and time, we have decided to compute cell area-mean dynamic and microphysical characteristics at each time and height within a defined radius of influence focused on the identified cell center locations. In this manner, comparisons will be made within a common area relative to the cell center for all cells. Several horizontal radii of influence ranging from 2.5 km to 10 km were examined using the CRM data, and it was determined that generating cell statistics over all grid points within a 4.0 km horizontal radius of the cell centers provided sufficient representation without potential contamination from nearby cells. Figure 3 provides two examples (from the RAMS Low-Aero simulation) of azimuthally averaged composite cell characteristics that change in magnitude with distance from cell centers. Both the total hydrometeor mixing ratio (top panel) and upward vertical velocity (bottom panel) fields demonstrate that the maxima of these fields are greatest at the centers (0.0 km) and lie well within 4.0 km horizontal distance of the composite cell centers. As such, the 4.0 km horizontal radius sufficiently encompasses the bulk dynamic and microphysical quantities of the identified cells while excluding features that may not be associated with the specific cells of interest. Use of the 4.0 km radius may also include cloud edges (that experience entrainment evaporation) that may have otherwise been excluded if using a smaller radius of influence in the analysis.

d. Cell compositing for comparative analysis

Cell composites of a population of cells within a given simulation for a chosen variable, such as updraft speed or cloud water mixing ratio, were then generated by the following process: (1) compute the mean of all horizontal grid points for a given variable with values greater than a designated threshold for each altitude within 4.0 km horizontal radius of each cell center and at each time in the lifetime of each cell; (2) take these area-mean values for each cell at each altitude and time and distribute them across a normalized cell lifetime; (3) take the mean of all identified cells in a simulation at each altitude and normalized time to generate cell composite means for each altitude and normalized cell time.

The cell composite means computed in step 3 are not thresholded, such that zero values in the time-height arrays are considered when compositing together the individual cell "thresholded means" from step 1. Compositing in this manner without thresholding prevents the means from being potentially dominated by a few strong cells. These cell-composited variables

represent the mean characteristics for each height and normalized time for the population of cells

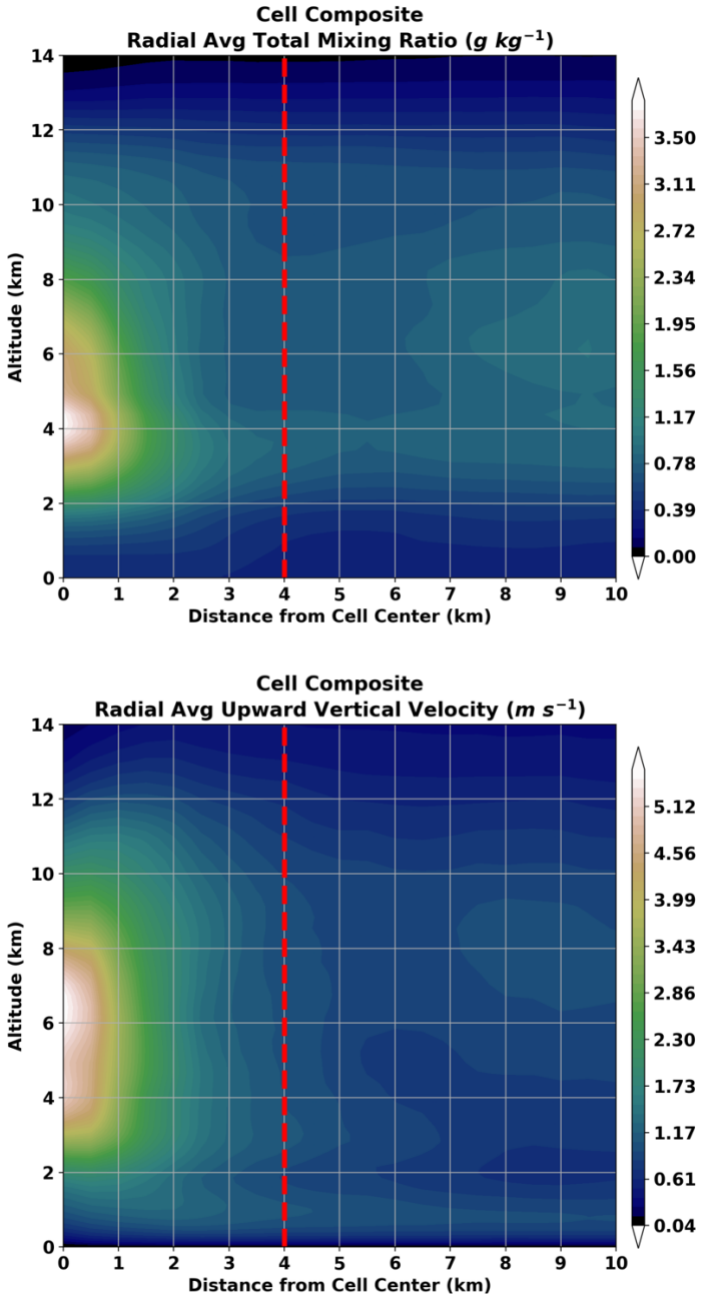

Figure 3. Composite radial profiles of (top) total hydrometeor mixing ratio (g kg^{-1}) and (bottom) upward vertical velocity (m s^{-1}) from the RAMS model Low-Aero simulation. Quantities were azimuthally averaged with distance from identified cell center locations, and the closest 10 km to cell centers are shown here. Composites incorporate the filtered cells identified in figure 1 and output times over the cell lifetimes. Examples from the other MIP models and the High-Aero simulations exhibit similar patterns, with the peaks of the variables readily contained within 4.0 km of the cell centers (noted by the vertical red, dashed line). Beyond about 5 km from the cell centers there is potential contamination of features not associated with the identified cells, hence the secondary maxima noted between 8-10 km from the composite cell center.

in each individual simulation. These can then be displayed as cell composite time-height diagrams to aid in the MIP inter-model comparison and Low vs High aerosol comparisons.

Given the nature of the scattered convection in this case study, as noted in M21, and a relatively low-shear southern Texas environment in late June, we do not suspect that there was much tilt to the cells/updrafts. Further, sampling the cylindrical area within 4 km horizontal distance of cell centers would encompass areas of minor tilt. Figure 3b in the manuscript suggests that the cell cores we are sampling in the tracking algorithm are generally upright.

3. Cell Composite Analyses

a. Discussion of cell composite figures

The cell composites in Figures 4 and 6-11 are all displayed in a similar format, and so we will take a moment to discuss the layout in detail. Each of these figures is divided into two components. The top half of the figures consists of time-height plots of cell composites of a given quantity from the Low-Aero simulations from each of the eight MIP CRMs. The altitude (km, AGL) is shown on the ordinate axis and the normalized cell lifetime on the abscissa. A cell's normalized time of 0.0 is the first time a cell is identified and 1.0 is the last time a cell is identified. This method permits a comparison of cell evolution independent of its absolute lifetime. The contouring at the 80^{th} percentile, denoted by the yellow line contour, was chosen subjectively to aid in visually focusing on the areas of greatest value. For the remainder of the discussion, we will refer to the area inside the yellow contours as the "peak zone" for that particular variable and CRM. The bottom half of the figures displays the corresponding differences in a particular variable that occurs due to aerosol loading, and it is computed as High-Aero minus Low-Aero. As such, the red (blue) colors indicate an increase (a decrease) in a given quantity due to an increase in aerosol concentration. In the composite cell analyses that follow, discussion and emphasis will be largely focused on the results from the CRM simulations that contained greater numbers of cells (see Figs. 1,2). Cell composites generated from simulations with very few cells (e.g., COSMO and ICON) are more likely to be biased by a few cells with outlier characteristics. We will still consider these models in the discussion, but caution is advised in placing their results in the context of the cell composites that include many more sampled cells.

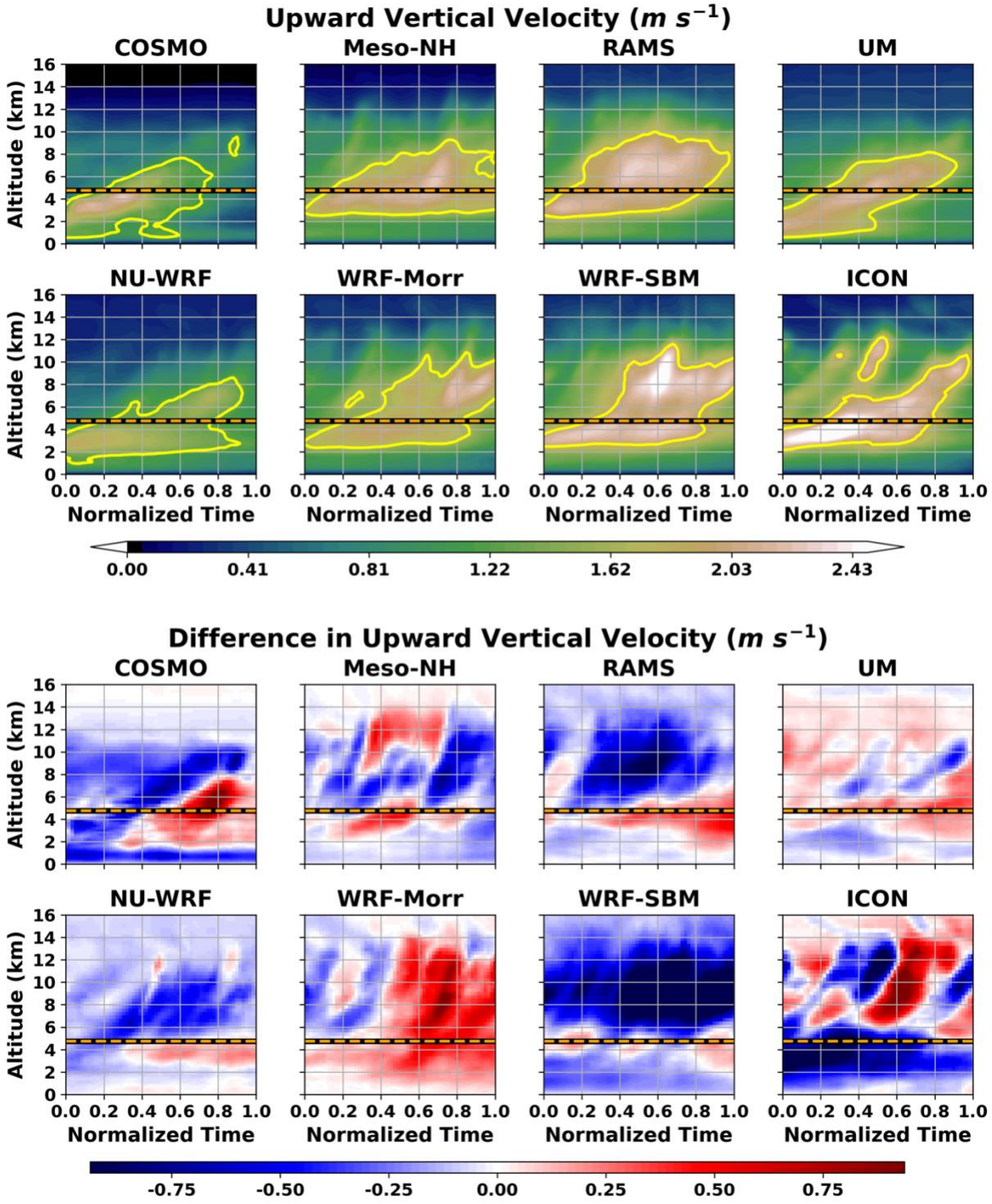

Figure 4. Time-height cross-sections of cell composites of mean updraft speed (m s^{-1}) from the Low-Aero simulations (top set), and the difference fields taken as High - Low Aero (bottom set). Time is on a normalized cell lifetime scale where 0.0 (1.0) is the first (last) identified cell time. Common color scales are based on the minimum/maximum values among all models. Yellow line contour outlines the 80th percentile. Horizontal black/orange line indicates the 0° C level.

b. Upward Vertical Velocity

Before proceeding toward the microphysical analysis, we first examine the tracked cell composite upward vertical velocity as a function of normalized cell lifetime (Fig. 4). In the top half of Figure 4, all of the CRMs display a growth in updraft depth (denoted by the height of the yellow contours indicating the depth of the peak zone) over cell lifetime with several of them topping out around 10-11 km AGL. Most of the CRMs then show a reduction in updraft strength, relative to the CRM's maximum, toward the end of cell lifetime. It is worth noting that these composites may miss the earliest and latest stages of cell lifetime since those stages cannot be captured by the mid-level updraft threshold used for cell identification and tracking. These cell composite updraft features, in conjunction with the number of identified cells in Figure 1, offer agreement with M21 which showed updraft Contour Frequency by Altitude Diagrams (CFADs) indicating fewer and shallower updrafts in COSMO and UM and more numerous and deeper updrafts in RAMS and WRF-SBM. It is encouraging that these varying analysis methods lead us to draw similar conclusions regarding updraft frequency and depth analysis, while the cell composite method further allows us to look at the mean evolution of the cells over their lifetime. We should also note that the analyses herein include cells of various depth as long as they meet the mid-level updraft speed threshold criteria (for identification and tracking) and $W > 3$ m s^{-1} reaches at least 6 km AGL within the cell during its lifetime.

In turning our attention to the bottom half of Figure 4, we examine the aerosol impact on the cell composite updrafts. There is substantial variability over cell lifetime between increases and decreases in updraft speed as well as in the vertical distribution. One common theme can be seen in the areas of increased updraft speed (the red shaded areas); most of the MIP CRMs display an increase in updraft strength below the 0°C level (~ 4.75 km AGL) where enhanced cloud condensation would tend to occur in association with aerosol loading and generation of a greater population of smaller cloud droplets (to be examined further below). While this is not a universal characteristic (see ICON and UM), it does follow the trends found in M21 in which enhanced updrafts appeared notably most consistent below the 0°C level. This was attributed in M21 to both aerosol invigoration as well as dynamic feedbacks to the environment, via enhanced instability related to a warmer boundary layer and a cooler low to mid-level layer related to entrainment evaporation, that could make stronger low-level updrafts more favorable. The increases in mid-level updraft strength are also most prevalent toward the mid to latter half of

cell lifetimes, which suggests that secondary nucleation and additional condensation may help drive stronger updrafts later in the cell lifetime, which could suggest more rapid dissipation in these cells.

Most of the CRMs also reveal reduced updraft speeds above ~ 6 km AGL (similar to M21), which suggests that aerosol invigoration by latent heat of freezing (to be examined further below) may be lacking. Greater evaporation/sublimation rates and reduced riming rates in High-Aero runs within the CRMs (that do not use saturation adjustment) may contribute to reduced updrafts aloft. Further, a water vapor deficit at mid to upper levels, as indicated in M21, resulting from enhanced low-level condensation may also contribute to weaker updrafts aloft. As such, we may expect to see less ice generated in these areas aloft where updraft speeds are reduced in polluted conditions. As shown in Figure 4, the models that use saturation adjustment (WRF-Morr, COSMO, UM, Meso-NH, ICON) are exceptions to this updraft reduction aloft, as they display various alternating periods of increased and decreased updraft speed over the composite cell lifetimes. This may be attributed to their constrained aerosol schemes, constant aerosol profile, and/or forced condensation on more fixed cloud droplet distributions (that also impact ice concentrations). We will revisit these varying trends in the aerosol impacts in the sections to follow, as changes in updrafts can be closely tied to changes in the resulting microphysical characteristics through changes in updraft induced supersaturations.

c. Cloud Water Composites

Changes in aerosol concentration from the Low-Aero to High-Aero environments most directly impacts the cloud droplet population by increasing the droplet number concentration, and subsequently, reducing the mean droplet size. Figure 5 displays time-averaged vertical profiles of cloud droplet mean mass diameter from each CRM for their respective Low and High aerosol simulations. The mean diameters are shown here in a single panel since there was minimal time variability and for ease of comparison among the CRM low and high aerosol simulations. All of the CRMs experience a sizable decrease in mean droplet size as aerosol concentration is increased. This reduction in droplet size can then impact the cloud water mixing ratio field via modifications to the autoconversion and accretion rates comprising the warm rain process, as well as riming rates that impact ice-phase hydrometeors. While the aerosol impact on the droplet mean diameters are consistent among CRMs, there is variability in the absolute sizes.

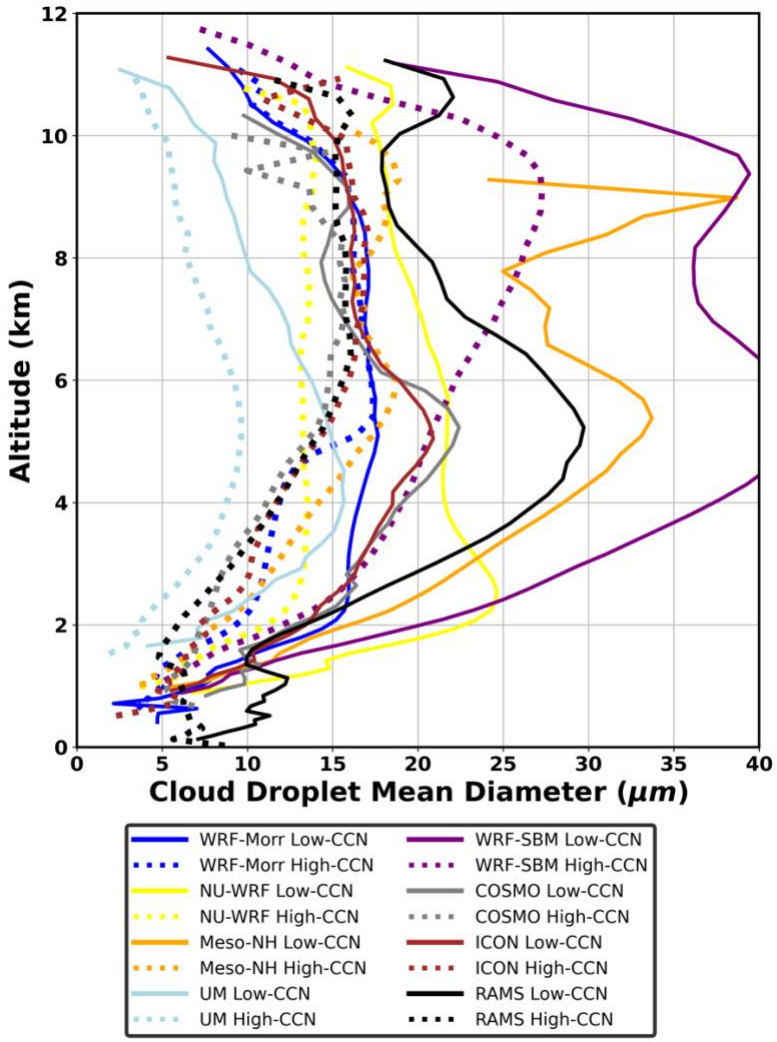

Figure 5. Vertical profiles of cloud droplet mean mass diameter (microns) within tracked cells. Results from each MIP model are color shaded with Low-Aero (High-Aero) results denoted by solid (dotted) lines.

This results from differences among CRMs with respect to their aerosol and droplet nucleation parameterizations, explicit activation vs saturation adjustment, and auto-conversion schemes.

The time-height cell composites of cloud water mixing ratio and its change due to aerosol loading are shown in Figure 6. There are broad similarities among all of the CRMs in the Low-Aero simulations (top half of Fig. 6) as highlighted by the yellow contoured peak zones in the figure subplots. Nearly all of the CRMs indicate the peak zone between 2-6 km AGL with the maximum cloud water occurring between 3-4 km AGL. The maximum in cloud water tends to peak within the first 40% of cell lifetime for all CRMs and decreases to a minimum value by the end of cell lifetime. Toward the end of cell lifetimes, ice-phase microphysics becomes more

425 active (to be shown below), and updrafts start to weaken and have reduced support for continued
426 cloud droplet formation and growth. Among CRMs we find that COSMO and ICON have the
427 greatest cell composite cloud water mixing ratio. However, these CRMs also had the fewest
428 identified cells that were likely relatively intense (i.e., greater updraft speed) and contained fewer
429 weak cells that could otherwise drive down the composite values. Absolute cloud base, denoted
430 by the minimum contour shading, shows that RAMS has the lowest minimum cloud base while
431 UM has the highest. This results from differences in the model thermodynamics such that RAMS
432 (UM) has a lower (higher) lifting condensation level (LCL). Though not shown, a near surface
433 analysis revealed that UM is about 2°C warmer than RAMS; differences in the initialization
434 dataset (See M21, Table A1) or radiation and land surface parameterizations may lead to these
435 temperature differences. The differences in surface temperature contribute to the differences in
436 LCL and cloud base. Regardless, the cell composite cloud layer depths, timing and duration, and
437 location of maxima exhibit close similarities among CRMs.
438 The bottom half of Figure 6 displays the aerosol-induced differences in cloud water
439 mixing ratio for the CRMs. While there are subtle differences in the details, all of the CRMs
440 produce an increase in cloud water in response to aerosol loading. In most of the CRMs this
441 increase is present throughout the cell lifetimes and is most commonly maximized during the
442 middle portion of cell lifetime, corresponding to the period with the strongest vertical motion.
443 The common increase in cloud water with aerosol loading is maximized from
444 approximately the upper portion of the cloud water peak zone and upward by 1-2 km AGL. As
445 such, an increased aerosol concentration leads to a raising of the height of the cloud water layer
446 and deepens it in some cases. Each CRM also reveals a thin blue shaded layer beneath the
447 increase shown as the deeper red shaded layer. The blue shade indicates a local decrease in cloud
448 water, which indicates that the lower portion of the cloud water layer has risen or thinned when
449 shifting to the High-Aero scenario. The rising of the cloud base can be explained by the warmer
450 and drier environments in the High-Aero scenarios that result from aerosol-induced reductions in
451 precipitation compared to the Low-Aero scenarios, which are discussed in M21 and represent
452 one of the many microphysical-dynamical feedbacks in cloud systems. This cloud layer
453 deepening results from reduced warm rain conversion and mixed-phase riming as well. Thus,
454 cloud water is not as readily scavenged and can be lofted higher in the updraft.

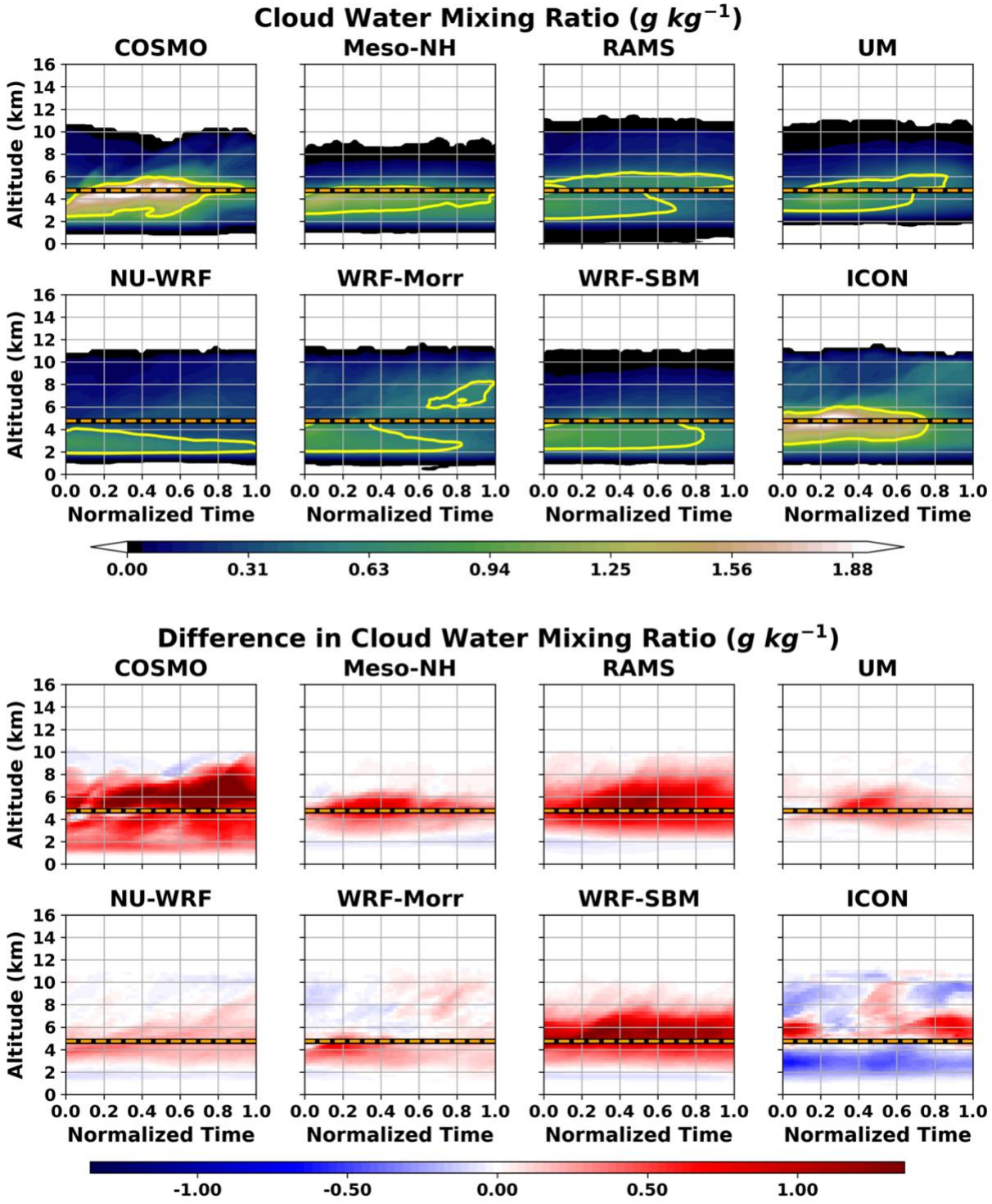

Figure 6. Same as figure 4, but for cloud water mixing ratio (g kg^{-1}).

d. Rain Water Composites

Like the cloud water composites, the rain water composites (Fig. 7) also reveal some consistency among the CRMs. The peak zones in the rain layers tend to fall between 2-5 km AGL, with some minor variability between CRMs. The rain mixing ratio, relative to each CRM's maximum, increases over time toward a peak during the middle of the composite cell lifetime and then dissipates toward the end. The normalized time of the peak in rain mixing ratio does vary between CRMs, with NU-WRF and WRF-Morr, for example, peaking around 0.4 and ICON peaking towards 0.75. Given the general consistency among CRMs in the timing of the peaks in cloud water (Fig. 6), it is the variability among microphysics schemes with respect to the efficiency of warm rain processes, as well as melting of ice, that is driving the differences in the timing of the rainwater peaks.

The aerosol effect on rain water production (bottom half of Fig. 7) is quite consistent among many of the CRMs (shown by the dominant blue shading), similar to what was seen for cloud water (shown by the dominant red shading in the bottom half of Fig. 6). For most of the CRMs, there is a clear overall decrease in rain water production, due to aerosol loading, over a deep layer from the surface up to near 6 km AGL. Some CRMs (NU-WRF, ICON) show a deep change in rain water up to 8 km AGL, though their relative maxima in difference tends to be from 4-5 km AGL. The magnitudes of the differences in rain water vary among CRMs (denoted by the degree of blue shading) as does the timing of the peaks during the cell lifetimes, which is largely determined by the overall amount of cloud water generated and the efficiency with which it is converted to rain as well as contribution from melting of ice. Shown in Figure 8, melting rates from most of the CRMs peaks over the final 40% of cell lifetime (after ice has had time to form, grow, and fall below the 0°C level), with lesser impacts earlier than this. Furthermore, most of the CRMs experience a decrease in melting of ice for an increase in aerosol concentration (bottom of Fig. 8), which results from reduced ice formation (to be discussed below with Fig. 9) and growth due to reduced riming efficiency associated with smaller cloud droplets. As such, both decreases in warm rain conversion (mostly in the early stages of cell lifetime) and melting (mostly in the latter stages of cell lifetime) contribute toward the overall reduction in rain water and associated surface precipitation. The notable increase in rain water in WRF-Morr (red shading, bottom half Fig. 7) over the final 40% of cell lifetime is associated with a greater overall contribution of melted ice (Fig. 8, WRF-Morr) to the amount of rain compared

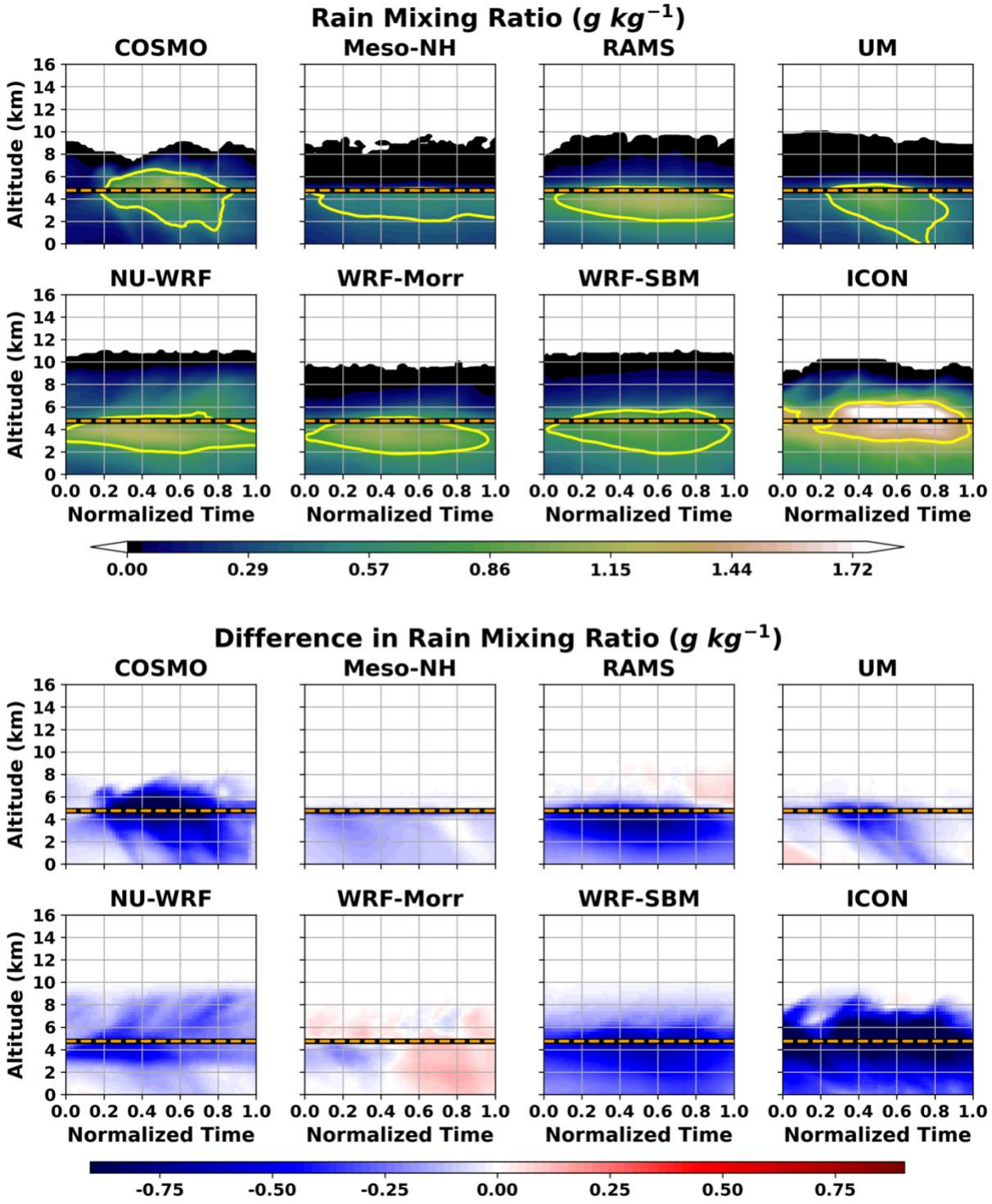

Figure 7. Same as figure 4, but for rain mixing ratio (g kg^{-1}).

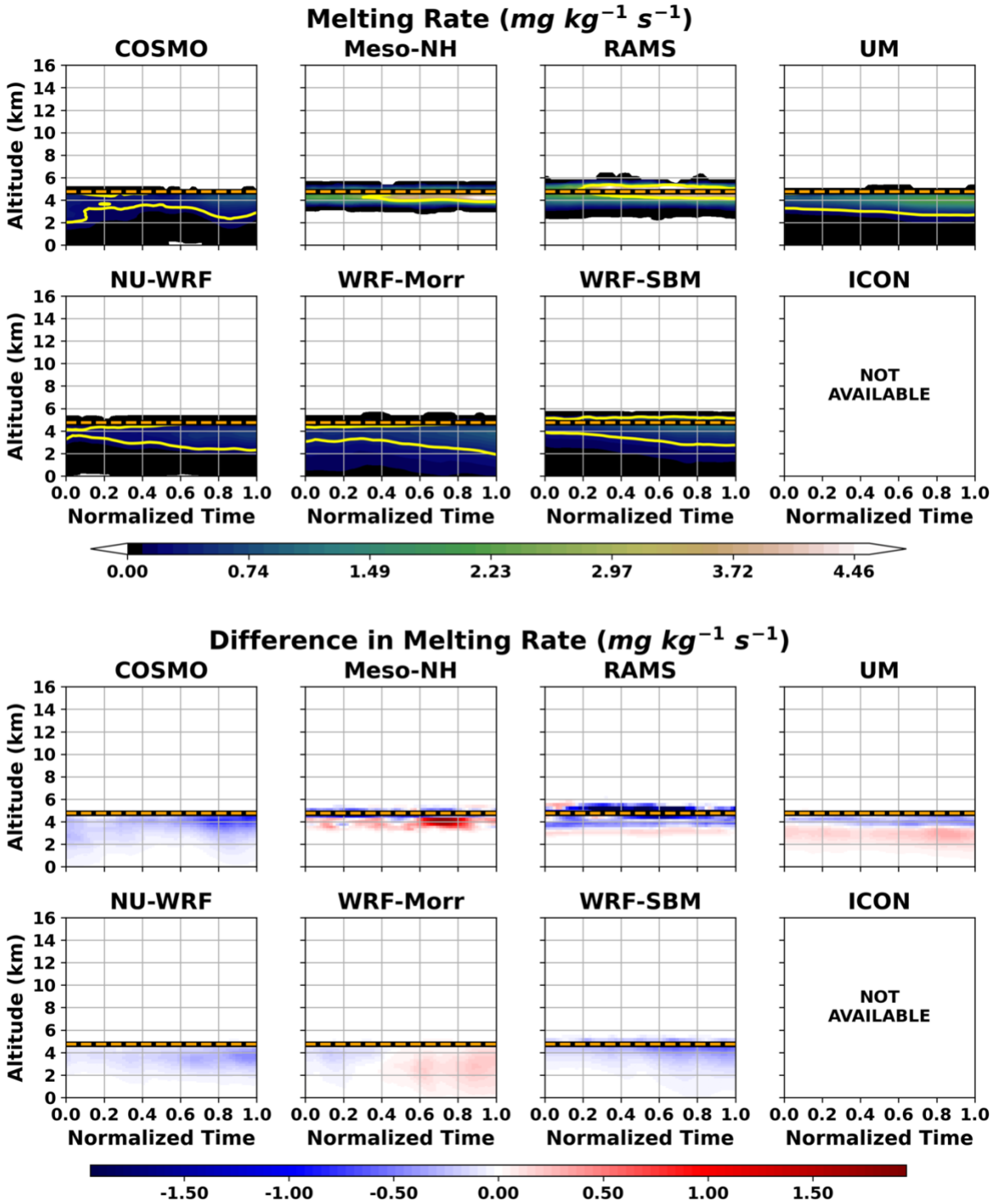

Figure 8. Same as figure 4, but for total ice species melting rate (mg kg^{-1} s^{-1}).

to warm rain processes, especially since the melting contribution is greatest in the latter stages of cell lifetimes. This scenario in WRF-Morr also corresponds with stronger updrafts and more ice through enhanced riming (to be discussed) during the latter stages of cell lifetime in response to aerosol loading which could be related to the constant aerosol profile and saturation adjustment interactions. A balance of these contributions to rain water, which are a function of cell lifetime, ultimately determines the overall change in rainwater in each respective microphysics scheme.

e. Ice Hydrometeor Composites

The cell composites of total ice hydrometeor mixing ratio (sum of all ice species) are displayed in Fig. 9, and they reveal a more complicated picture compared to the fields of updraft speed, cloud water, and rain water. Ice hydrometeor mixing ratio includes a sum of all ice hydrometeor species available in each CRM. The top half of Figure 9 shows cell composites of total ice, from each CRM's Low-Aero simulation. These vary substantially among CRMs with respect to depth of the ice maxima, duration and timing of the CRM-relative maxima, peak vertical location of ice layer maxima, and the amount of ice mixing ratio.

Of the CRMs that contain cells with substantial ice (Meso-NH, RAMS, UM, WRF-Morr, WRF-SBM) most of them display their ice maxima toward the latter half of the cell composite lifetime, lying somewhere between 0.6 and 0.9 of the cell lifetimes, thereby lagging the warm-phase hydrometeor development. Among these same CRMs with substantial ice, the depths of the ice layers (as indicated by contoured peak zones) vary more than that of cloud or rain water. It should also be noted that several of the CRMs (WRF-Morr, WRF-SBM, ICON) have minor amounts of ice that reach the surface in the form of hail. While these are relatively small amounts of surface ice, this is in contrast to a couple of the other CRMs that do not have any ice below about 3 km AGL (Meso-NH, RAMS). These differences point toward variability in hail, melting rates, low-level temperature, and fall speeds, all of which vary among the CRMs.

The indirect aerosol impact on total ice (bottom of Fig. 9) is also more variable than that of updraft speed, cloud water, and rain water among the CRMs. The aerosol induced changes in ice broadly suggest a reduction in ice in most of the CRMs due to aerosol loading as indicated by more area of blues (decreases) in the composite subplots. There is more variability in ice over the cell depth and lifetime (denoted by varying red and blue patterns in the subplots) compared to the previous cell composites. This points toward greater variability in mixed-phase and ice process

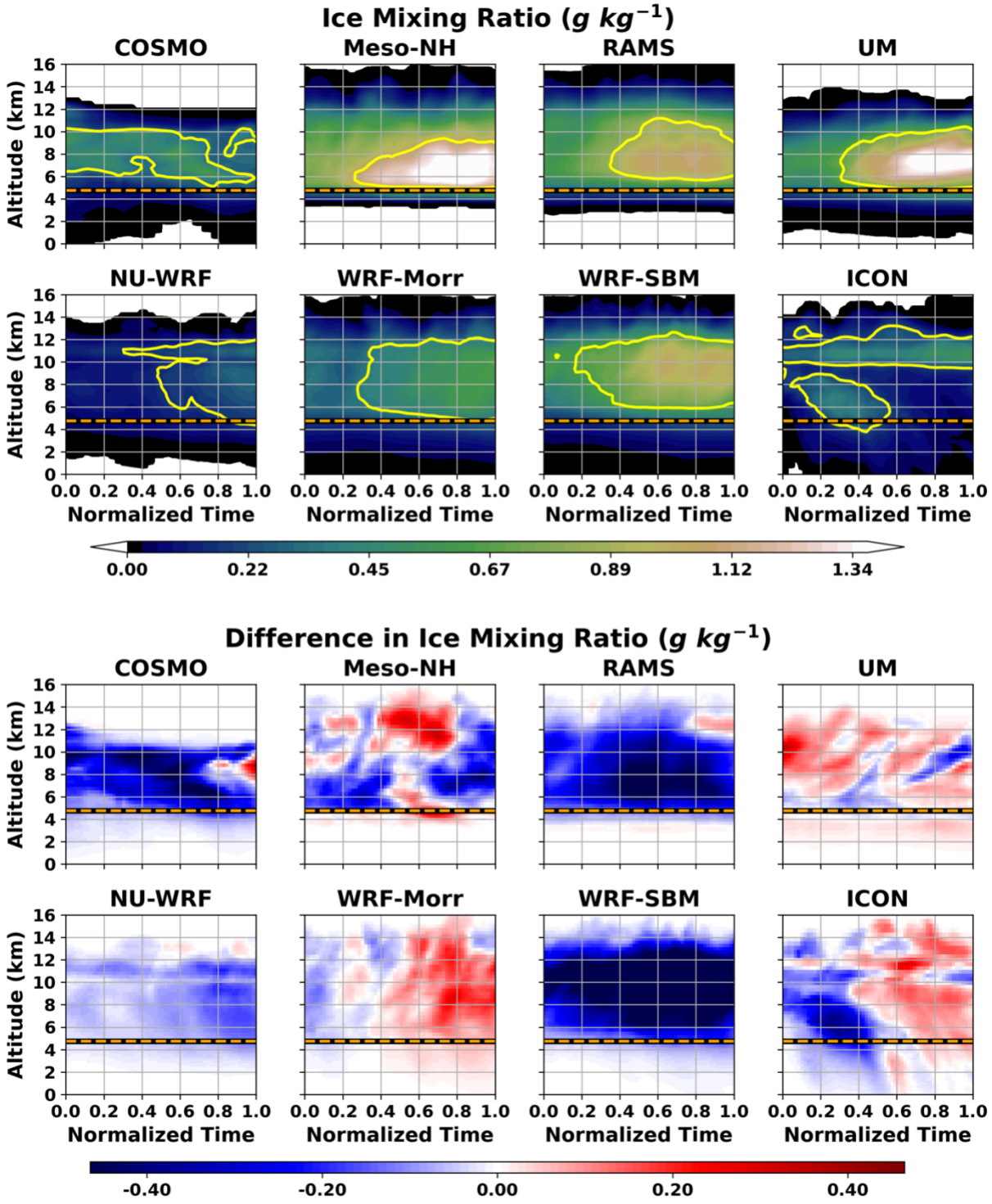

Figure 9. Same as figure 4, but for total ice mixing ratio (g kg^{-1}).

rates among CRMs, as discussed above, when aerosol concentration is altered. This variability may also alter feedbacks to the cells that can impact potential cell deepening.

WRF-SBM is most consistent with respect to the decrease in ice in the High-Aero case, and (bottom half of Fig. 9) it reveals an overall decrease in ice over a deep layer and over the full duration of the cell lifetime. A brief look back at the cloud droplet mean diameters (Fig. 5) shows that WRF-SBM experiences the greatest reduction in cloud droplet size among all the CRMs. This leads to increased evaporation and sublimation rates along cloud edges where entrainment effects are important. This also contributes to a consistent decrease in ice via less efficient rime accretion processes. While more cloud water remains for riming in the High-Aero scenarios (bottom of Fig. 6) (due to reduced conversion to rain), the reduced cloud droplet sizes may limit the amount of rime contribution to ice production. As such, the predicted change in cloud droplet sizes in the various CRMs contributes to the amount of change in rime growth. For a given updraft strength, CRMs with a greater reduction in cloud droplet size may see a greater or more consistent reduction in rime growth and ice mass compared to others; furthermore, the various methods of parameterizing rime growth also contribute to these differences in ice. While most of the CRMs did not provide riming rates as diagnostic variables, both RAMS and WRF-Morr (not shown) which did provide these riming rates, with RAMS indicating predominant reduction in riming rates from 5-10 km AGL in response to the increase in aerosol concentration and with WRF-Morr indicating reduced riming in the first half of cell lifetime and increased riming in the second half of cell lifetime. The aerosol related changes in riming rates track with the changes in upper-level updrafts, ice production, and melting.

The greater variability in ice among the CRMs as well as over the vertical extent and cell lifetimes within the convective cells of each CRM, points toward the complexity of simulating ice processes and the variability among the parameterizations of mixed-phase and ice-phase particle growth mechanisms as well as their feedbacks to cell development.

f. Latent Heating Composites

The peak zones of latent heating (top of Fig. 10) tend to broadly coincide with the similar zones in the updraft plots (Fig. 4). However, most of the CRMs have a peak latent heating zone that is less deep than the updraft peak zone depth by at least 2 km. Latent heating contributes to buoyancy production to help drive updraft accelerations, but it is only one of several contributing

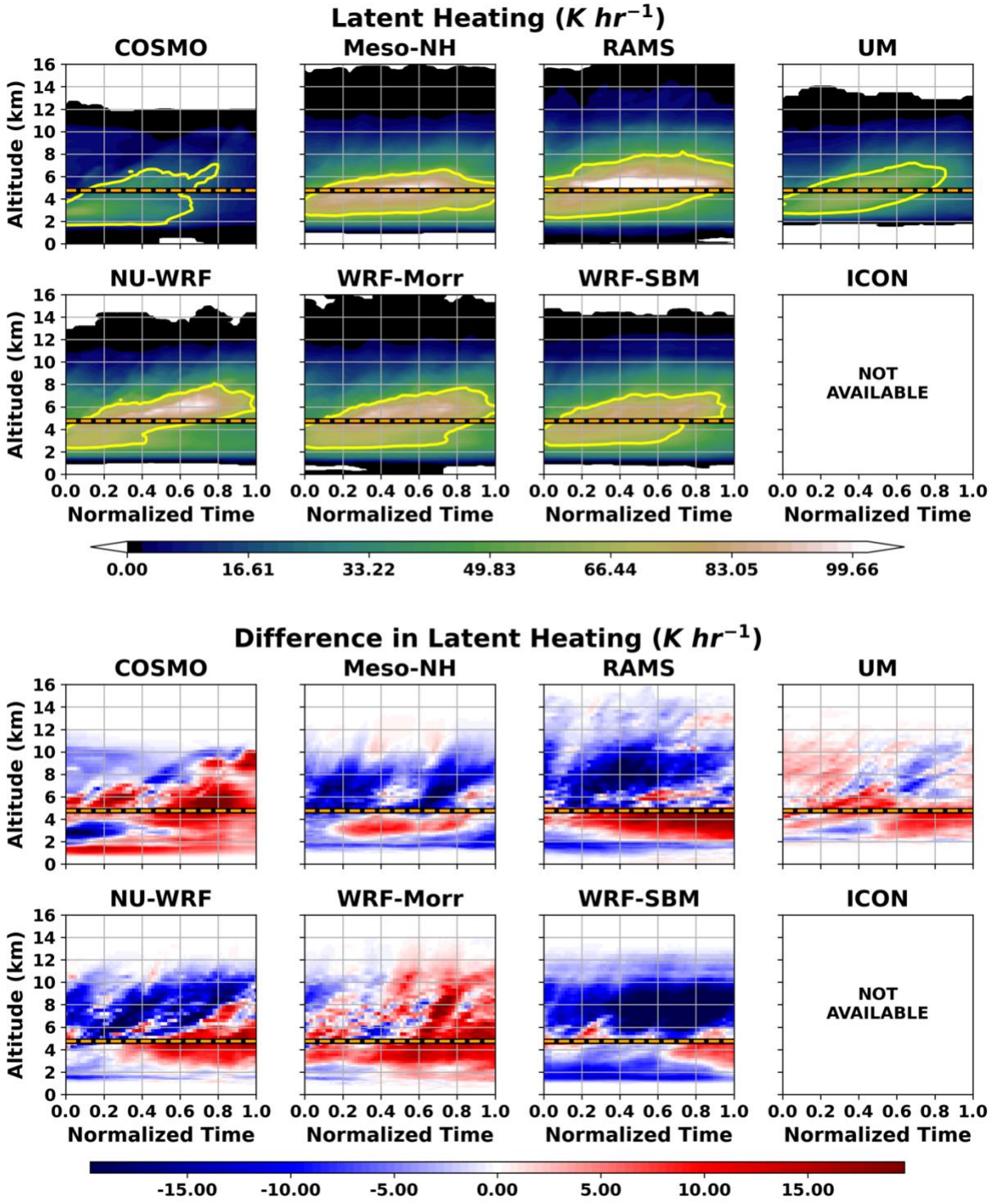

Figure 10. Same as figure 4, but for latent heating rate (K hr^{-1}).

processes to updraft strength. (M21 provides a detailed analysis of the role of buoyancy production and the vertical pressure gradient force to the vertical momentum equation.) The updraft and latent heating peak zones most notably overlap in the warm-phase regions of the cell composites with the latent heating zone tapering off with altitude as one moves upward into the mixed-phase zone of the cells above the 0°C level (~ 4.75 km AGL). Latent heating rates are closely tied to updrafts through condensation and vapor deposition growth of hydrometeors, as well as freezing when cloud and rain drops are rimed or freeze homogeneously. The release of latent heat can then contribute to buoyancy production and feedback to the updraft as a source of acceleration. Most of the CRMs experience an increase in height or depth of the peak zone of latent heating over cell lifetime followed by a reduction or decay toward the last 20% of the lifetime. This is also in keeping with the trend in the lifecycle of cell updrafts, though the peak zones in latent heating are not nearly as deep. Since the latent heat of condensation is nearly an order of magnitude greater than that of freezing, the peak zones of total latent heating are concentrated in the warm-phase regions of the cells. As such, there is a tapering off of the peak zone of latent heating above the peak zone of cloud water as condensation rates decrease higher aloft where cloud mixing ratio is reduced (Fig. 6).

The aerosol impact on latent heating (bottom of Fig. 10) reveals a consistent pattern within most of the CRMs, whereby, there is an increase in latent heating rate (denoted by the red shaded layers) roughly coinciding with the liquid cloud layer and region of increased cloud water (Fig. 6) in the High-Aero scenario that is persistent over the cell lifetimes. This indicates a consistent increase in condensation associated with an increase in cloud water. In the High-Aero scenario, in the CRMs that do not use a saturation adjustment scheme, a greater population of smaller cloud droplets increases the effective droplet surface area for condensation growth, and thus, latent heat release. Though not shown here, the CRMs that provided microphysical process rates of vapor condensation, reveal an overlapping pattern, over cell lifetime and cell depth, of enhanced condensation and latent heating in the High-Aero simulations. In addition, most of the CRMs display reduced latent heating above the 0°C level that is typically persistent over cell lifetimes in most CRMs, however, three of the CRMs that use saturation adjustment exhibit an increase in latent heating over a deeper layer. The CRMs that display a more consistent reduction in ice (Fig. 9) also display a more consistent reduction in latent heating in the cold phase region of the cells. The aerosol-induced differences in latent heating very closely follow the aerosol-

induced difference of updrafts.

Feedback mechanisms among aerosols, microphysics, and dynamics contribute to the trends noted above. In the High-Aero scenario more numerous, smaller clouds droplets are generated. Due to reduced autoconversion, these are less likely to become rain drops. Instead, they continue to grow by condensation, all the while releasing more latent heat particularly later in the cell lifetime due to delayed or reduced autoconversion. This provides the fuel for sustaining or strengthening updrafts later into the cell lifecycle. In addition, as noted previously from M21, in these simulations, reduced precipitation in the High-Aero cases prevents stabilization of the boundary layer which acts as a positive feedback that permits higher cloud base and stronger updrafts. Clouds that develop further and extend upwards into the mixed-phase zone may continue to grow by condensation and further release latent heat well into the mixed-phase zone. However, since the droplets in the High-Aero simulations are still quite small compared to the Low-Aero simulations, riming rates (and thus, freezing rates) are reduced, so there is not a significant contribution to latent heating from the freezing process. As such, the amount of ice is reduced. And since there is less overall ice, there are fewer ice hydrometeor sites for freezing or deposition growth. Thus, there is reduced overall latent heating in the upper-mixed-phase and cold phase zones of the cells in most of the CRMs. The CRMs with more aerosol-induced variability in the ice field over cell depth and lifetime display more variability in the latent heating above the 0°C level.

g. Latent Cooling Composites

Latent cooling rates result from the combined phase changes associated with melting, evaporation, and sublimation. The peak zones of latent cooling in the Low-Aero scenarios (top half of Fig. 11) in most of the CRMs are concentrated near the cloud water peak layer and 0°C level. As noted earlier, in most of the CRMs, cloud water is most dominant during the first half of the cell lifetimes, while ice amounts peak during the second half of cell lifetimes. As such, the peak zones of latent cooling tend to be more associated with cloud droplet evaporation (due to entrainment along cloud edges or near cloud base) peaking during the formative stages of the cells and with contributions from ice hydrometeor melting and sublimation and rain evaporation (along cloud edges) during the latter portion of cell lifetimes. Given that our cell sampling region was within 4 km of cell centers, it is possible that some cloud edges were not included; however,

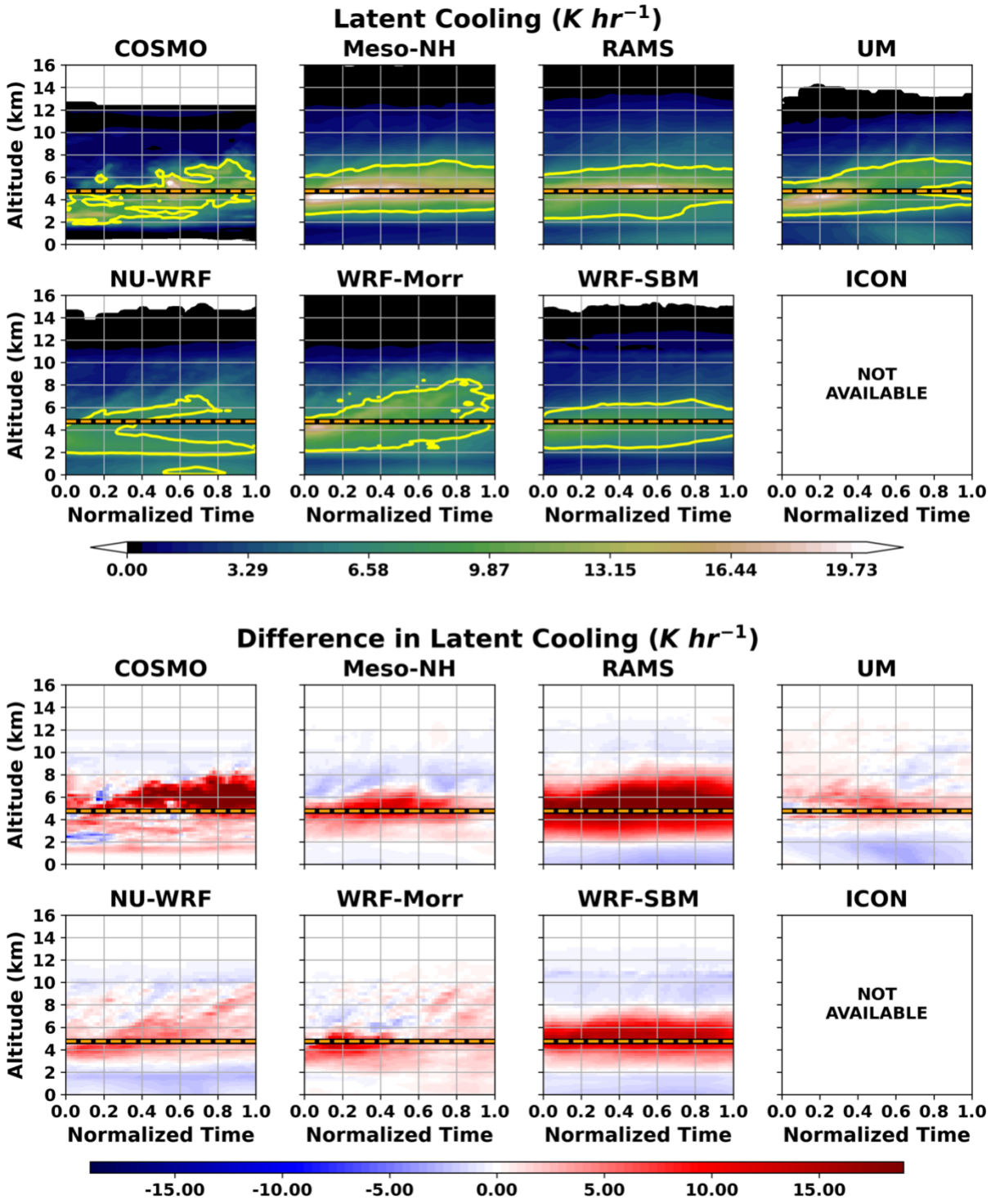

Figure 11. Same as figure 4, but for latent cooling rate (K hr^{-1}).

640 the presence of latent cooling that is coincident with the cloud layer indicates that entrainment
641 evaporation was occurring in the sampled regions either by cloud edge or cloud base droplet
642 evaporation in a substantial number of cells.
643 Most of the CRMs also show secondary maxima in latent cooling near the surface where
644 rain evaporation is maximized below cloud base in the second half of the cell lifetime. This
645 process plays a key role in generating cold pools and stabilizing the boundary layer. NU-WRF
646 appears to have the greatest relative contribution from sub-cloud rain evaporation for this given
647 event; however, the extension of the peak zone to the surface would not have appeared if the
648 mean latent cooling magnitude had been a bit greater in the primary cloud and melting layers.
649 The aerosol impacts on latent cooling (bottom half of Fig. 11) are generally confined
650 within two layers in the majority of the CRMs, and they are largely consistent over cell lifetimes.
651 For an increase in aerosol concentration, there is a prominent increase in cooling above the
652 boundary layer at cloud layer elevations (noted by the bright red shaded regions) associated with
653 the increase in cloud water (seen in the bottom panels of Fig. 6). The presence of more
654 numerous, smaller cloud droplets leads to an enhancement of cloud edge or cloud base net
655 evaporation that contributes to the zone of increased latent cooling. Melting also contributes to
656 latent cooling (Fig. 8), but it is a smaller contributor than droplet evaporation, and it was found to
657 be largely reduced in the High-Aero cases since less ice is typically present.
658 The enhanced cooling from cloud edge evaporation at high aerosol concentration may
659 contribute toward the reduction in upper-level ice and limit potential convective invigoration.
660 Considering the large reduction in droplet size and the large increase in latent cooling from the
661 Low- to High-Aero cases, it is possible that the High-Aero case has the aerosol concentration
662 exceeding the optimal aerosol concentrations for convection invigoration, as previous studies
663 showed, such that the large evaporative cooling in this situation could lead to a strong
664 suppression of convection and precipitation (e.g., Fan et al., 2007 and Li et al., 2008).
665 The other prominent feature in most of the CRMs is the blue shaded latent cooling region
666 near the surface within the lowest 2 km AGL that is consistent over cell lifetime. This results
667 from a decrease in sub-cloud evaporation of rain due to a general reduction in rain formation in
668 the High-Aero case, as noted in the discussion of rain water in association with Fig. 7. In general,
669 the latent cooling rates tend to be dominated by the warm-phase processes with some addition
670 from the narrow melting layer toward the end of cell lifetimes.

4. Summary and Conclusions

In this follow-on study from M21 and V25 we have utilized the case study simulations of deep convection from the ACPC MIP, that included 8 state-of-the-art CRMs, in order to examine the impacts of increased aerosol concentration on composite convective cell microphysical properties and their variability over cell lifecycles. This case was characterized by ordinary convection over the Houston, TX (USA) region from 19-20 June 2013. The overarching investigation of this case by V25 assessed the general variability of simulated convection among the CRMs as well as the impacts of aerosol loading on convective clouds, their microphysical characteristics, and accumulated precipitation. M21 focused on the impacts of increasing aerosol concentration on convective updrafts, in these same CRMs, over a 12-hour period from 1600 UTC 19 June – 0400 UTC 20 June with 5-minute model output. Convective columns were identified using established convection partitioning criteria, and various metrics were used for comparing updraft statistics, and their modification by aerosol loading among the MIP CRMs.

In this current effort, we have focused our attention on a 3-hour period of convection from 2100 UTC 19 June – 0000 UTC 20 June 2013 for which 1-minute CRM output was available. The *tobac* cell tracking algorithm was applied to the high frequency output from the CRMs to identify and track mid-level updrafts exceeding thresholds of 3, 5, and 10 m s^{-1}. Using tracked cell location output from *tobac*, cells with lifetimes of 20-60 minutes and updrafts that extended above the 0°C level to at least 6 km AGL were included in generating composite cell properties (computed as means at each vertical level within a 4 km horizontal radius of cell centers) of various microphysical and dynamic fields for each CRM's Low and High aerosol simulations. All identified cells within a given simulation were mapped to a normalized time scale to generate time-height composites for comparing CRMs and Low and High aerosol scenarios.

The variability in cell composite updrafts and microphysical properties among the CRMs and Low to High aerosol scenarios revealed a number of consistent trends worth discussing. The altitude vs normalized-time cell composites of updraft speed (Fig. 4) displayed a range of updraft depth among CRMs and over cell lifetimes with the contoured peak zones reaching maximum altitudes from 5 to 12 km AGL. Most of the CRMs reveal an increase in updraft peak zone depth from initial cell detection toward the end of cell-detectable lifetime. There is variability among CRMs as to the timing of maximum updraft strength, though most of them reach their maximum

between 40-80% of the cell lifetime and then display reduced updraft strength toward the very end of the identified cell lifetime. The aerosol impact on updraft strength tended to result in increases in updraft speed in the warm-phase to lower mixed-phase regions of the cells that were most prevalent toward the mid to latter half of cell lifetimes, which suggests that secondary nucleation and additional condensation may help drive stronger updrafts later in the cell lifetime, which could suggest more rapid dissipation in these cells. Trends were mixed and less consistent aloft in the upper mixed-phase and cold-phase regions of the cells. In spite of the different analysis methods, these results tend to agree with the analysis of aerosol impacts on updrafts in M21.

Cell composites of cloud and rain water mixing ratio (Figs. 6,7) reveal rather consistent representations across the CRMs with the peak zones of cloud and rain covering very similar depths and lifetimes. All of the CRMs display a delay in the onset of rain over the cell lifetime compared to the development of the cloud layer, though there is some inter-model variability in the timing of the maximum rain mixing ratio. This results from both the model-specific rates of the autoconversion and accretion of cloud water and the melting of ice (Fig. 8) contributing to rain toward the end of cell lifetimes. The aerosol impact on cloud and rain water is also quite consistent among most of the CRMs. Generally, there is a consistent increase in cloud water as aerosol concentration is increased, and the cloud layer lifts to a slightly higher altitude. These effects result from reduced autoconversion and accretion processes that transfer cloud droplets to precipitation-sized rain drops, as well as feedbacks from environmental changes due to reduced rainfall, as noted in M21. Likewise, rain water is consistently reduced among most CRMs over all depths and throughout the cell lifetimes, due largely to the aforementioned reduction in collision-coalescence growth of cloud droplets and raindrops. The peak in the reduction in rain during the cell lifetimes tends to coincide with the timing of the greatest amount of rainwater. A reduction in melted ice (Fig. 8) also contributes to the aerosol-induced reduction in rain.

From an inter-model view, the cell composites of the total ice hydrometeor mixing ratio (Fig. 9) reveal a different scenario when compared to cloud and rain water. There is greater variability among CRMs with respect to the duration, depth, and location and timing of maxima in the peak zones of ice mass mixing ratio, though most of the CRMs place the ice maxima during the second half of cell lifetimes after cells have had time to deepen and mixed- and cold-phase processes become active. There is also more variability in the cell composite total ice

maxima among the CRMs than in cloud and rain water. This variability speaks strongly to the CRM differences in ice-phase microphysical processes that generate initial ice embryos and then transfer liquid hydrometeors to ice hydrometeors through freezing and riming processes. Differences in the individual parameterizations of these processes have a profound effect on the overall generation of ice among the CRMs. The aerosol impact on ice is also highly variable over the cell depth and lifecycle among the CRMs compared to that seen for cloud and rain water.

The cell composites of latent heating (Fig. 10) reveal similarities among the CRMs as seen in the comparisons of cloud and rain water composites. The timing of the increase in latent heating and deepening of the latent heating peak zones in the cell composites follows that of the updrafts. Further, the CRMs show a general increase in latent heating in association with the increase in cloud water production following an increase in aerosol concentration. This is typically maximized over the latter half of cell lifetimes. The overall latent heating profiles and their responses to aerosol loading are dominated by warm-phase microphysics with lesser contribution from mixed and cold phases processes. Latent cooling (Fig. 11) was also similar among the CRM cell composites, generally persistent over cell lifetimes, and was dominated by cloud edge droplet evaporation rather than melting. Secondary zones of near-surface raindrop evaporation were also apparent. Aerosol loading led to increased cloud edge evaporation and reduced near-surface rain evaporation in all of the CRMs.

This study, along with M21 and V25, have laid the groundwork for future MIP studies and have identified areas of agreement among models and areas that need additional investigation and improvement. The various CRMs in this study are most consistent with respect to warm-phase microphysics and are most different regarding mixed and cold-phase clouds and microphysical processes. Our goal moving forward is to continue to identify areas of scientific and modeling uncertainty associated with deep convection, isolate the causes of the uncertainty, and devise solutions to reduce these uncertainties. Collaborative efforts, such as undertaken in this current MIP, are highly productive means of achieving these goals.

A follow-on MIP associated with cases identified from the Tracking Aerosol Convection Interactions Experiment (TRACER; Jensen et al. 2019), with an intense observation period from June - September of 2022 in the Houston, TX area, is being planned (https://arm-synergy.github.io/tracer-mip/Roadmap.html). This TRACER-MIP will seek to expand on our knowledge gained from this ACPC-MIP. The TRACER-MIP will simulate multiple case study

764 days of isolated convection (in varying thermodynamic environments) over the Houston area for
765 which in-situ and remote sensing observations were readily available for assistance in model
766 initialization and validation.
767
768 *Acknowledgements.*
769 This analysis was supported by the Department of Energy Atmospheric System Research grants
770 DE-SC0021160 and DE-SC0012704. WRF-SBM efforts were supported by the Argonne
771 National Laboratory's Science Focus Area. The COSMO simulations at KIT were performed on
772 the supercomputer ForHLR funded by the Ministry of Science, Research and the Arts Baden-
773 Württemberg and by the Federal Ministry of Education and Research. For the ICON simulations,
774 this work used resources of the Deutsches Klimarechenzentrum (DKRZ) granted by its Scientific
775 Steering Committee (WLA) under project 1143. RC and JQ acknowledge funding by the
776 "PATTERA" project (FKZ 01LP1902C) as part of the "ClimXtreme" project funded by the
777 German Ministry of Education and Research (Bundesministerium für Bildung und Forschung,
778 BMBF) in its strategy "Research for Sustainability" (FONA).
779
780 *Data Availability Statement.*
781 The ACPC MIP deep convection CRM simulation data used in this analysis are available from
782 the UK NERC JASMIN data analysis facility in the ACPC group workspace. Individuals can
783 apply for a JASMIN account at the following site: https://jasmin.ac.uk/users/access/. For easier
784 access, we suggest that those interested in accessing the CRM data contact
785 peter.marinescu@colostate.edu or stephen.saleeby@colostate.edu. The source code and
786 documentation for the Tracking and Object-Based Analysis of Clouds (tobac), used for cell
787 tracking in this study, are available at https://github.com/climate-processes/tobac (Heikenfeld et
788 al., 2019a).
789

790 ## 5. References

791 Abbott, T. H. and T.W. Cronin, 2021: Aerosol invigoration of atmospheric convection through
792 increases in humidity. *Science*, **371**, 83-85.
793
794 Albrecht, B. A., 1989: Aerosols, Cloud Microphysics, and Fractional Cloudiness. *Science (80).*,
795 **245**, 1227–1230, https://doi.org/10.1126/science.245.4923.1227.
796
797 Altaratz, O., I. Koren, L. A. Remer, and E. Hirsch, 2014: Review: Cloud invigoration by
798 aerosols—Coupling between microphysics and dynamics. *Atmos. Res.*, **140**–**141**, 38–60,
799 https://doi.org/10.1016/j.atmosres.2014.01.009.
800
801 Andreae, M. O., D. Rosenfeld, P. Artaxo, A. A. Costa, G. P. Frank, K. M. Longo, and M. A. F.
802 Silva-Dias, 2004: Smoking rain clouds over the Amazon, *Science*, **303**, 1337–1342.
803 https://doi.org/10.1126/science.1092779
804

Barrett, A. I., and C. Hoose, 2023: Microphysical Pathways Active Within Thunderstorms and Their Sensitivity to CCN Concentration and Wind Shear. *J. Geophys. Res. Atmos.*, **128**, https://doi.org/10.1029/2022JD036965.

Cheng, C.-T., W.-C. Wang, and J.-P. Chen, 2010: Simulation of the effects of increasing cloud condensation nuclei on mixed-phase clouds and precipitation of a front system. *Atmos. Res.*, **96**, 461–476, https://doi.org/10.1016/j.atmosres.2010.02.005.

Cheng, C., W. Wang, and J. Chen, 2007: A modeling study of aerosol impacts on cloud microphysics and radiative properties. *Q. J. R. Meteorol. Soc.*, **133**, 283–297, https://doi.org/10.1002/qj.25.

Cotton, W. R., and Coauthors, 2003: RAMS 2001: Current status and future directions. *Meteorol. Atmos. Phys.*, **82**, 5–29, https://doi.org/10.1007/s00703-001-0584-9.

Dipankar, A., B. Stevens, R. Heinze, C. Moseley, G. Zängl, M. Giorgetta, and S. Brdar, 2015: Large eddy simulation using the general circulation model ICON. *J. Adv. Model. Earth Syst.*, **7**, 963–986, https://doi.org/10.1002/2015MS000431.

Fan, J., D. Rosenfeld, Y. Ding, L. R. Leung, and Z. Li, 2012: Potential aerosol indirect effects on atmospheric circulation and radiative forcing through deep convection, *Geophys. Res. Lett.*, **39**, Article No. L09806. https://doi.org/10.1029/2012GL051851

Fan, J., L. R. Leung, D. Rosenfeld, Q. Chen, Z. Li, J. Zhang, and H. Yan, 2013: Microphysical effects determine macrophysical response for aerosol impacts on deep convective clouds. *Proc. Natl. Acad. Sci.*, **110**, E4581–E4590, https://doi.org/10.1073/pnas.1316830110.

Fan, J., R. Zhang, G. Li, and W.-K. Tao, 2007: Effects of aerosols and relative humidity on cumulus clouds. *J. Geophys. Res.*, **112**, D14204, https://doi.org/10.1029/2006JD008136.

Fan J., B. Han, A. Varble, H. Morrison, et al., 2017: Cloud-resolving model intercomparison of an MC3E squall line case: Part I—Convective updrafts, *J. Geophys. Res. Atmos*., **122**, 9351–9378, https://doi.org/10.1002/2017JD026622.

Fan, J., and Coauthors, 2018: Substantial convection and precipitation enhancements by ultrafine aerosol particles. *Science*, **359**, 411–418, https://doi.org/10.1126/science.aan8461.

Field, P. R., and Coauthors, 2023: Implementation of a double moment cloud microphysics scheme in the UK met office regional numerical weather prediction model. *Q. J. R. Meteorol. Soc.*, **149**, 703–739, https://doi.org/10.1002/qj.4414.

Grabowski, W. W., and H. Morrison, 2016: Untangling Microphysical Impacts on Deep Convection Applying a Novel Modeling Methodology. Part II: Double-Moment Microphysics. *J. Atmos. Sci.*, **73**, 3749–3770, https://doi.org/10.1175/JAS-D-15-0367.1.

Heikenfeld, M., P. J. Marinescu, M. Christensen, D. Watson-Parris, F. Senf, S. C. van den Heever, and P. Stier, 2019: tobac 1.2: towards a flexible framework for tracking and analysis of clouds in diverse datasets. *Geosci. Model Dev.*, **12**, 4551–4570, https://doi.org/10.5194/gmd-12-4551-2019.

Heikenfeld, M., B. White, L. Labbouz, and P. Stier, 2019: Aerosol effects on deep convection: the propagation of aerosol perturbations through convective cloud microphysics. *Atmos. Chem. Phys.*, **19**, 2601–2627, https://doi.org/10.5194/acp-19-2601-2019.

Igel, A. L., and S. C. van den Heever, 2021: Invigoration or Enervation of Convective Clouds by Aerosols? *Geophys. Res. Lett.*, **48**, https://doi.org/10.1029/2021GL093804.

Ilotoviz, E., A. P. Khain, N. Benmoshe, V. T. J. Phillips, and A. V. Ryzhkov, 2016: Effect of Aerosols on Freezing Drops, Hail, and Precipitation in a Midlatitude Storm. *J. Atmos. Sci.*, **73**, 109–144, https://doi.org/10.1175/JAS-D-14-0155.1.

Jensen, M. P., 2019: Tracking Aerosol Convection Interactions Experiment (TRACER) science plan. Brookhaven National Laboratory Tech. Rep. BNL-212068-2019-INRE, 41pp.

Kaufman, Y. J., and T. Nakajima, 1993: Effect of Amazon Smoke on Cloud Microphysics and Albedo-Analysis from Satellite Imagery. *J. Appl. Meteorol.*, **32**, 729–744, https://doi.org/10.1175/1520-0450(1993)032<0729:EOASOC>2.0.CO;2.

Khain, A., and A. Pokrovsky, 2004: Simulation of Effects of Atmospheric Aerosols on Deep Turbulent Convective Clouds Using a Spectral Microphysics Mixed-Phase Cumulus Cloud Model. Part II: Sensitivity Study. *J. Atmos. Sci.*, **61**, 2983–3001, https://doi.org/10.1175/JAS-3281.1.

Khain, A., D. Rosenfeld, and A. Pokrovsky, 2005: Aerosol impact on the dynamics and microphysics of deep convective clouds. *Q. J. R. Meteorol. Soc.*, **131**, 2639–2663, https://doi.org/10.1256/qj.04.62.

Khain, A., D. Rosenfeld, A. Pokrovsky, U. Blahak, and A. Ryzhkov, 2011: The role of CCN in precipitation and hail in a mid-latitude storm as seen in simulations using a spectral (bin) microphysics model in a 2D dynamic frame. *Atmos. Res.*, **99**, 129–146, https://doi.org/10.1016/j.atmosres.2010.09.015.

Koren, I., Y. J. Kaufman, D. Rosenfeld, L. A. Remer, and Y. Rudich, 2005: Aerosol invigoration and restructuring of Atlantic convective clouds. *Geophys. Res. Lett.*, **32**, L14828, doi:10.1029/2005GL023187.

Koren, I., G. Dagan, and O. Altaratz, 2014: From aerosol-limited to invigoration of warm convective clouds. *Science (80-.).*, **344**, 1143–1146, https://doi.org/10.1126/science.1252595.

Korolev, A. and Leisner, T, 2020: Review of experimental studies of secondary ice production, *Atmos. Chem. Phys.*, **20**, 11767–11797, https://doi.org/10.5194/acp-20-11767-2020.

Lac, C., and Coauthors, 2018: Overview of the Meso-NH model version 5.4 and its applications. *Geosci. Model Dev.*, **11**, 1929–1969, https://doi.org/10.5194/gmd-11-1929-2018.

Leuenberger, D., M. Koller, O. Fuhrer, and C. Schär, 2010: A Generalization of the SLEVE Vertical Coordinate. *Mon. Weather Rev.*, **138**, 3683–3689, https://doi.org/10.1175/2010MWR3307.1.

Lowenthal, D. H., R. D. Borys, W. Cotton, S. Saleeby, S. A. Cohn, and W. O. J. Brown, 2011: The altitude of snow growth by riming and vapor deposition in mixed-phase orographic clouds. *Atmos. Environ.*, **45**, 519–522, https://doi.org/10.1016/j.atmosenv.2010.09.061.

Marinescu, P. J., S. C. van den Heever, S. M. Saleeby, and S. M. Kreidenweis, 2016: The microphysical contributions to and evolution of latent heating profiles in two MC3E MCSs. *J. Geophys. Res. Atmos.*, **121**, 7913–7935, https://doi.org/10.1002/2016JD024762.

Marinescu, P. J., and Coauthors, 2021: Impacts of Varying Concentrations of Cloud Condensation Nuclei on Deep Convective Cloud Updrafts—A Multimodel Assessment. *J. Atmos. Sci.*, **78**, 1147–1172, https://doi.org/10.1175/JAS-D-20-0200.1.

Marinescu, P. J., S. C. van den Heever, S. M. Saleeby, S. M. Kreidenweis, and P. J. DeMott, 2017: The Microphysical Roles of Lower-Tropospheric versus Midtropospheric Aerosol Particles in Mature-Stage MCS Precipitation. *J. Atmos. Sci.*, **74**, 3657–3678, https://doi.org/10.1175/JAS-D-16-0361.1.

Mlawer, E. J., S. J. Taubman, P. D. Brown, M. J. Iacono, and S. A. Clough, 1997: Radiative transfer for inhomogeneous atmospheres: RRTM, a validated correlated-k model for the longwave. *J. Geophys. Res. Atmos.*, **102**, 16663–16682, https://doi.org/10.1029/97JD00237.

Morrison, H., 2012: On the robustness of aerosol effects on an idealized supercell storm simulated with a cloud system-resolving model. *Atmos. Chem. Phys.*, **12**, 7689–7705, https://doi.org/10.5194/acp-12-7689-2012.

Morrison, H., and W. W. Grabowski, 2011: Cloud-system resolving model simulations of aerosol indirect effects on tropical deep convection and its thermodynamic environment. *Atmos. Chem. Phys.*, **11**, 10503–10523, https://doi.org/10.5194/acp-11-10503-2011.

Morrison, H., M. van Lier-Walqui, A. M. Fridlind, W. W. Grabowski, J. Y. Harrington, C. Hoose, et al. 2020: Confronting the challenge of modeling cloud and precipitation microphysics. *Journal of Advances in Modeling Earth Systems*, 12, e2019MS001689. https://doi.org/10.1029/2019MS001689

939 Oktem, R., D.M. Romps, and A.C. Varble, 2023: No warm-phase invigoration of convection
940 detected during GoAmazon. J. Atmos. Sci., 80, 2345-2364. https://doi.org/10.1175/JAS-D-
941 22-0241.1
942
943 Peters-Lidard, C. D., and Coauthors, 2015: Integrated modeling of aerosol, cloud, precipitation
944 and land processes at satellite-resolved scales. *Environ. Model. Softw.*, **67**, 149–159,
945 https://doi.org/10.1016/j.envsoft.2015.01.007.
946
947 Pinsky, M., L. Magaritz, A. Khain, O. Krasnov, and A. Sterkin, 2008: Investigation of Droplet
948 Size Distributions and Drizzle Formation Using a New Trajectory Ensemble Model. Part I:
949 Model Description and First Results in a Nonmixing Limit. *J. Atmos. Sci.*, **65**, 2064–2086,
950 https://doi.org/10.1175/2007JAS2486.1.
951
952 Rosenfeld, D., 1999: TRMM observed first direct evidence of smoke from forest fires inhibiting
953 rainfall. *Geophys. Res. Lett.*, **26**, 3105–3108, https://doi.org/10.1029/1999GL006066.
954
955 Rosenfeld, D., and Coauthors, 2014: Global observations of aerosol-cloud-precipitation-climate
956 interactions. *Rev. Geophys.*, **52**, 750–808, https://doi.org/10.1002/2013RG000441.
957
958 Rosenfeld, D., U. Lohmann, G. B. Raga, C. D. O'Dowd, M. Kulmala, S. Fuzzi, A. Reissell, and
959 M. O. Andreae, 2008: Flood or Drought: How Do Aerosols Affect Precipitation? *Science*,
960 **321**, 1309–1313, https://doi.org/10.1126/science.1160606.
961
962 Rosenfeld, D., and W. L. Woodley, 2000: Deep convective clouds with sustained supercooled
963 liquid water down to -37.5 °C. *Nature*, **405**, 440–442, https://doi.org/10.1038/35013030.
964
965 Saleeby, S. M., S. C. Van Den Heever, P. J. Marinescu, S. M. Kreidenweis, and P. J. DeMott,
966 2016: Aerosol effects on the anvil characteristics of mesoscale convective systems. *J.*
967 *Geophys. Res.*, **121**, 10,880-10,901, https://doi.org/10.1002/2016JD025082.
968
969 Saleeby, S. M., S. R. Herbener, S. C. van den Heever, and T. L'Ecuyer, 2015: Impacts of Cloud
970 Droplet–Nucleating Aerosols on Shallow Tropical Convection. *J. Atmos. Sci.*, **72**, 1369–
971 1385, https://doi.org/10.1175/JAS-D-14-0153.1.
972
973 Saleeby, S. M., and S. C. van den Heever, 2013: Developments in the CSU-RAMS Aerosol
974 Model: Emissions, Nucleation, Regeneration, Deposition, and Radiation. *J. Appl. Meteorol.*
975 *Climatol.*, **52**, 2601–2622, https://doi.org/10.1175/JAMC-D-12-0312.1.
976
977 Schättler, U., G. Doms, and C. Schraff, 2019: A description of the nonhydrostatic regional
978 COSMO-model—Part VII: User's guide. COSMO Doc., 181 pp., http://www.cosmo-
979 model.org/.
980
981 Sheffield, A. M., S. M. Saleeby, and S. C. van den Heever, 2015: Aerosol-induced mechanisms
982 for cumulus congestus growth. *J. Geophys. Res. Atmos.*, **120**, 8941–8952,
983 https://doi.org/10.1002/2015JD023743.
984

Shpund, J., and Coauthors, 2019: Simulating a Mesoscale Convective System Using WRF With a New Spectral Bin Microphysics: 1: Hail vs Graupel. *J. Geophys. Res. Atmos.*, **124**, 14072–14101, https://doi.org/10.1029/2019JD030576.

Skamarock, W. C., and Coauthors, 2008: A description of the Advanced Research WRF version 3. NCAR Tech. Note NCAR/TN- 4751STR, 113 pp., https://doi.org/10.5065/D68S4MVH

Sokolowsky, G. A., S. W. Freeman, and S. C. van den Heever, 2022: Sensitivities of Maritime Tropical Trimodal Convection to Aerosols and Boundary Layer Static Stability. *J. Atmos. Sci.*, **79**, 2549–2570, https://doi.org/10.1175/JAS-D-21-0260.1.

Sokolowsky, G. A., Freeman, S. W., Jones, W. K., Kukulies, J., Senf, F., Marinescu, P. J., Heikenfeld, M., Brunner, K. N., Bruning, E. C., Collis, S. M., Jackson, R. C., Leung, G. R., Pfeifer, N., Raut, B. A., Saleeby, S. M., Stier, P., and van den Heever, S. C.: tobac v1.5: introducing fast 3D tracking, splits and mergers, and other enhancements for identifying and analysing meteorological phenomena. *Geosci. Model Dev.*, **17**, 5309–5330, https://doi.org/10.5194/gmd-17-5309-2024.

Squires, P., 1958: The Microstructure and Colloidal Stability of Warm Clouds. *Tellus*, **10**, 256–261, https://doi.org/10.1111/j.2153-3490.1958.tb02011.x.

Storer, R. L., and S. C. van den Heever, 2013: Microphysical Processes Evident in Aerosol Forcing of Tropical Deep Convective Clouds. *J. Atmos. Sci.*, **70**, 430–446, https://doi.org/10.1175/JAS-D-12-076.1.

Tao, W.-K., X. Li, A. Khain, T. Matsui, S. Lang, and J. Simpson, 2007: Role of atmospheric aerosol concentration on deep convective precipitation: Cloud-resolving model simulations. *J. Geophys. Res.*, **112**, D24S18, https://doi.org/10.1029/2007JD008728.

Tao, W.-K., J.-P. Chen, Z. Li, C. Wang, and C. Zhang, 2012: Impact of aerosols on convective clouds and precipitation. *Rev. Geophys.*, **50**, 2011RG000369, https://doi.org/10.1029/2011RG000369.

Teller, A., and Z. Levin, 2006: The effects of aerosols on precipitation and dimensions of subtropical clouds: a sensitivity study using a numerical cloud model. *Atmos. Chem. Phys.*, **6**, 67–80, https://doi.org/10.5194/acp-6-67-2006.

Twomey, S., 1977: The Influence of Pollution on the Shortwave Albedo of Clouds. *J. Atmos. Sci.*, **34**, 1149–1152, https://doi.org/10.1175/1520-0469(1977)034<1149:TIOPOT>2.0.CO;2.

Twomey, S., and P. Squires, 1959: The Influence of Cloud Nucleus Population on the Microstructure and Stability of Convective Clouds. *Tellus*, **11**, 408–411, https://doi.org/10.1111/j.2153-3490.1959.tb00050.x.

van den Heever, S. C., G. G. Carrió, W. R. Cotton, P. J. DeMott, and A. J. Prenni, 2006: Impacts of Nucleating Aerosol on Florida Storms. Part I: Mesoscale Simulations. *J. Atmos. Sci.*, **63**, 1752–1775, https://doi.org/10.1175/JAS3713.1.

van den Heever, S.C., and Coauthors, 2017: Aerosol-Cloud-Precipitation-Climate (ACPC) initiative: Deep Convective Cloud Group roadmap. ACPC Rep., 13 pp., http://acpcinitiative.org/Docs/ACPC_ DCC_Roadmap_171019.pdf.

van den Heever, S.C., P.J. Marinescu, M. Heikenfeld, B. White, A. Fridlind, P. Stier, M. Andreae, A. Barrett, C. Barthlott, R. Cherian, J. Fan, C. Hoose, T. Matsui, A. Miltenberger, J. Quaas, D. Rosenfeld, J. Shpund, B. Vie, Y. Zhang, and Stephen M. Saleeby 2024: A model intercomparison project exploring aerosol impacts on deep convective clouds. *Bull. Amer. Met. Soc.* (In internal revision.)

Varble, A., 2018: Erroneous attribution of deep convective invigoration to aerosol concentration, *J. Atmos. Sci.*, **75**, 1351–1368, https://doi.org/10.1175/JAS-D-17-0217.1

Veals, P. G., A.C. Varble, J.O.H. Russell, J. Hardin, and E. Zipser, 2022: Indications of a Decrease in the Depth of Deep Convective Cores with Increasing Aerosol Concentration during the CACTI Campaign. *J. Atmos. Sci*., **79**, 705-722, https://doi.org/10.1175/JAS-D-21-0119.1.

Walters, D., and Coauthors, 2017: The Met Office Unified Model Global Atmosphere 6.0/6.1 and JULES Global Land 6.0/6.1 configurations. *Geosci. Model Dev.*, **10**, 1487–1520, https://doi.org/10.5194/gmd-10-1487-2017.

Wang, C., 2005: A modeling study of the response of tropical deep convection to the increase of cloud condensation nuclei concentration: 2. Radiation and tropospheric chemistry. *J. Geophys. Res. Atmos.*, **110**, https://doi.org/10.1029/2005JD005829.

Zängl, G., D. Reinert, P. Rípodas, and M. Baldauf, 2015: The ICON (ICOsahedral Non-hydrostatic) modeling framework of DWD and MPI-M: Description of the non-hydrostatic dynamical core. *Q. J. R. Meteorol. Soc.*, **141**, 563–579, https://doi.org/10.1002/qj.2378.